

# Lawrence Berkeley National Laboratory

## LBL Publications

### Title

Detailed seismic imaging of the Mw 7.1 Ridgecrest earthquake rupture zone from data recorded by dense linear arrays

### Permalink

<https://escholarship.org/uc/item/54z3g9v8>

### Authors

Qiu, Hongrui  
Ben-Zion, Yehuda  
Catchings, RD  
[et al.](#)

### Publication Date

2020-10-31

### DOI

10.1002/essoar.10504611.1

### Copyright Information

This work is made available under the terms of a Creative Commons Attribution-NonCommercial License, available at <https://creativecommons.org/licenses/by-nc/4.0/>

1       **Seismic imaging of the Mw 7.1 Ridgecrest earthquake rupture zone from data**  
2                               **recorded by dense linear arrays**

3  
4  
5  
6

Hongrui Qiu<sup>1</sup>, Yehuda Ben-Zion<sup>2,3</sup>, Rufus Catchings<sup>4</sup>, Mark R. Goldman<sup>4</sup>, Amir A.  
Allam<sup>5</sup>, and Jamison Steidl<sup>4,6</sup>

7       <sup>1</sup>Department of Earth, Environmental and Planetary Sciences, Rice University, Houston, TX,  
8       USA

9       <sup>2</sup>Department of Earth Sciences, University of Southern California, Los Angeles, CA, USA

10      <sup>3</sup>Southern California Earthquake Center, University of Southern California, Los Angeles, CA,  
11      USA

12      <sup>4</sup>U.S. Geological Survey, 345 Middlefield Road MS 977, Menlo Park, California 94025-3591  
13      U.S.A

14      <sup>5</sup>Department of Geology and Geophysics, University of Utah, Salt Lake City, UT, USA

15      <sup>6</sup>Earth Research Institute, University of California, Santa Barbara, CA, USA

16  
17

18      Corresponding author: Hongrui Qiu ([hongruiq@rice.edu](mailto:hongruiq@rice.edu), [qiuhonrui@gmail.com](mailto:qiuhonrui@gmail.com))

19  
20

21      **Key points:**

- 22              • Several 1- to 2-km-wide low-velocity zones with more intensely damaged inner  
23              cores (0.5-1.5 km wide) are identified beneath each array
- 24              • An automated detector, based on peak ground velocities and durations of high  
25              amplitude *S* waves, identifies fault-zone trapped waves
- 26              • The *P* wave delay time and *S* wave amplification patterns indicate consistent  
27              locations and widths of fault damage zones

28 **Abstract**

29 We analyze seismograms recorded by four arrays (B1-B4) with 100-m station spacing  
30 and apertures of 4-8 km that cross the surface rupture of the 2019 Mw 7.1 Ridgecrest  
31 earthquake. The arrays extend from B1 in the northwest to B4 in the southeast of the  
32 surface rupture. Delay times between *P*-wave arrivals associated with ~1200 local  
33 earthquakes and four teleseismic events are used to estimate local velocity variations  
34 beneath the arrays. Both teleseismic and local *P* waves travel faster on the northeast than  
35 the southwest side of the fault beneath arrays B1 and B4, but the velocity contrast is less  
36 reliably resolved at arrays B2 and B3. We identify several 1- to 2-km-wide low-velocity  
37 zones with much slower inner cores that amplify *S* waveforms, inferred as damage zones,  
38 beneath each array. The damage zones at arrays B2 and B4 also generate fault-zone head  
39 and trapped waves. An automated detector, based on peak ground velocities and  
40 durations of high-amplitude waves, identifies candidate fault-zone trapped waves  
41 (FZTWs) in a localized zone for ~600 earthquakes at array B4. Synthetic waveform  
42 modeling of averaged FZTWs, generated by ~30 events with high-quality signals,  
43 indicates that the trapping structure at array B4 has a width of ~300 m, depth of 3-5 km,  
44 *S*-wave velocity reduction of ~20% with respect to the surrounding rock, *Q*-value of  
45 ~30, and *S*-wave velocity contrast of ~4% across the fault (faster on the northeast side).  
46 The results show complex fault-zone internal structures (velocity contrasts and low-  
47 velocity zones) that vary along fault strike.

48

49 **Plain Language Summary**

50 The 2019 Mw 7.1 Ridgecrest earthquake in the Eastern California Shear Zone generated  
51 a vigorous aftershock sequence that provided a wealth of seismic data. We derive  
52 subsurface structural properties within and across the Ridgecrest rupture zone from  
53 seismic waveforms generated by the earthquake sequence. The data are recorded by four  
54 dense nodal arrays that were deployed across the Ridgecrest rupture zone with ~100 m  
55 spacing and aperture of a few kilometers. Delay times of *P* wave and amplification of *S*  
56 waves are used to infer on several 1-2-km-wide low-velocity zones with more intensely  
57 damaged inner cores (0.5-1.5 km wide) beneath each array. Waveform modeling of fault

58 zone trapped waves well-recorded by one array provides geometrical and seismic  
59 properties of a coherent waveguide in the damage fault zone structure at that location.  
60 The results are complementary to tomographic models that provide a regional context but  
61 do not resolve internal structural elements of the Ridgecrest rupture zone.

62

## 63 **1. Introduction**

64 The Mw 7.1 Ridgecrest earthquake of July 5, 2019 and the earlier Mw 6.4 event on  
65 July 4 in the southern part of the Walker Lane shear zone (Fig. 1) were felt throughout  
66 southern California and produced a vigorous aftershock sequence. These events led to  
67 rapid deployments of seismic arrays across and around the Ridgecrest earthquake  
68 sequence (Catchings et al., 2020). Kinematic rupture processes of the Mw 6.4 and Mw  
69 7.1 events, surface deformation, and properties of the aftershocks show complex patterns,  
70 with strong variations both along strike of the rupture zones and in depth (e.g., Chen et  
71 al., 2020; Cheng & Ben-Zion, 2020; Jia et al., 2020; Ross et al., 2019; Xu et al., 2020).  
72 Data recorded by several dense arrays crossing the rupture zone of the Mw 7.1  
73 earthquake can be used to derive high-resolution seismic information on the internal  
74 structure of the rupture zone. Detailed imaging of the structure associated with the  
75 rupture zone can provide important information on various topics, including initiation and  
76 arrest of ruptures (e.g., Aki, 1979; King, 1986), amplification of seismic waves (e.g.,  
77 Kurzon et al., 2014; Rovelli et al. 2002; Spudich & Olsen, 2001), interactions of ruptures  
78 with fault zone properties (e.g., Ben-Zion & Huang 2002; Brietzke & Ben-Zion 2006;  
79 Huang et al., 2014), and properties of earthquake sequences (e.g., Thakur et al., 2020).

80 Several velocity models for the Ridgecrest area provide information for volumes with  
81 spatial resolutions ranging from several km (e.g., Lee et al., 2014; Shaw et al., 2015) to  
82 about 500 m (White et al. 2020). Structures in the top 1-2 km are poorly resolved in these  
83 velocity models due to limitations of the input data. Analyses of seismic data recorded by  
84 arrays across faults and rupture zones have proven highly effective in complementing  
85 regional velocity models and imaging sharp bimaterial interfaces and damage zones with  
86 width of a few tens of meters (e.g., Ben-Zion et al., 2003; Cochran et al., 2009; Li et al.,  
87 1994; Peng et al., 2003; Qin et al., 2018; Qiu et al., 2017; Share et al., 2019).

88 In this study, we investigate the seismic and geometrical properties of the damage  
89 structure associated with the 2019 Mw 7.1 Ridgecrest earthquake, based on the data  
90 obtained from four dense linear seismic arrays (B1-B4; triangles in Figs. 1 and 2) located  
91 across segments of the rupture. Analyses of the arrival patterns of *P* waves from both  
92 teleseismic and local seismic events across each array helps to detect and constrain  
93 properties of velocity contrasts across fault sections and low-velocity zones reflecting at  
94 least partially damaged rock. We identified fault-zone trapped waves, i.e., amplified  
95 motions of *S* waves associated with core damage zones that are sufficiently coherent to  
96 act as a waveguide, at some locations and inverted for average geometrical and seismic  
97 properties of the fault-zone waveguide.

98 In the following sections, we describe the deployment and data processing in section  
99 2 and present the methodology and results on various aspects of the fault-zone structures  
100 from different types of observations in section 3. The imaging results from different  
101 phases and analyses are summarized and discussed in section 4. The results show overall  
102 complex fault-zone structures that vary along the rupture strike, in general agreement  
103 with fault surface traces (Xu et al., 2020), seismic catalog (Ross et al., 2019) and potency  
104 of aftershocks (Cheng & Ben-Zion, 2020) in the Ridgecrest area.

105

## 106 **2. Data & basic processing**

107 Four linear arrays, with about 100-m station spacing and apertures of 4-8 km, were  
108 deployed across the surface rupture of the 2019 Mw 7.1 Ridgecrest earthquake (Fig. 1).  
109 The arrays extended from B1 in the northwest to B4 in the southeast of the surface  
110 rupture (Fig. 2). In total, the B-arrays consisted of 248 Fairfield and SmartSolo sensors  
111 that recorded continuously at 500 Hz for about a one-month period (7/12/2019-8/8/2019).

112 For teleseismic delay time analysis (Section 3.1), we use the Taup toolkit (Crotwell et  
113 al., 1999) and velocity model IASP91 (Kennett & Engdahl, 1991) for predictions of *P*-  
114 arrival time at each station. The teleseismic earthquakes have epicentral distances  
115 between 30-90°, depth > 50 km, and Mw > 6.0. For analysis of local *P* waves (Section  
116 3.2), we first extract the seismic waveforms generated by ~1200 local events (red box in  
117 Fig. 1) at each station and use the catalog of Hauksson et al. (2012, extended to 2019) for

118 locations. The mean and linear trend are removed from the waveforms, and a bandpass  
119 filter between 0.5 Hz and 20 Hz is applied. In the study of fault zone trapped waves  
120 (Section 3.3), the north-south and east-west components are rotated to a coordinate  
121 system parallel and perpendicular to the fault strike.

122

### 123 **3. Analysis**

124 We conduct three types of studies involving different signals and spatial scales to  
125 image several components of the fault-zone structure associated with the 2019 Mw 7.1  
126 Ridgecrest earthquake beneath the four linear arrays (Fig. 2). We describe the analyses  
127 below, starting with large-scale structural features (e.g., overall velocity variations across  
128 the fault) and progressing to inner fault-zone components (e.g., geometry and velocity of  
129 the damage zone). The results are obtained using teleseismic delay-time analyses (DTA),  
130 local *P*-wave DTA, and analysis associated with FZTWs following the *S*-wave arrival.

131

#### 132 3.1 Teleseismic delay time analysis

133 During the one-month deployment, teleseismic *P* waves with sufficient signal to noise  
134 ratios ( $\text{SNR} > 5$ ) between 0.5 Hz and 2 Hz were recorded for three events at array B1 and  
135 four earthquakes at arrays B2-B4 (Figs. S1- S4). We do not investigate teleseismic *S*  
136 waves since they have  $\text{SNR} < 5$ .

137

##### 138 *3.1.1 Methodology*

139 As shown in previous studies (e.g., Ozakin et al., 2012; Qiu et al., 2017), there are  
140 three contributing factors to travel-time delays observed on a linear array for a  
141 teleseismic arrival: the geometry between the incoming plane wave and the array,  
142 topography, and the crustal structure beneath the array. To obtain the travel-time delays  
143 due to local crustal structures, we first predict the arrival time of the teleseismic *P*-wave  
144 for each station and event pair using the IASP91 model and assume the station is at sea  
145 level. Then, teleseismic *P* waveforms are bandpass filtered between 0.5 Hz and 2 Hz. By  
146 aligning the teleseismic *P* waves with respect to the corresponding predicted arrival time  
147 (Fig. 3b) at each station, we remove the delay times associated with the non-vertical

148 incidence angle of incoming waves. This assumes a flat Moho interface beneath the  
 149 array, which is likely given the small area involved and receiver function results (e.g.,  
 150 Zhu & Kanamori, 2000).

151 In Qiu et al. (2017), the  $P$  waveform is first stacked over the entire array for a specific  
 152 teleseismic event and used as the reference. Then, the arrival-time pattern of  $P$  waves is  
 153 extracted from cross-correlations of the  $P$  waveform recorded at each station and the  
 154 reference waveform. However, this method is accurate only for arrays with short aperture  
 155 (e.g.,  $\sim 500$  m in Qiu et al., 2017) when  $P$ -wave delay times are small (e.g.,  $\sim 0.01$  s). For  
 156 arrays with long aperture, the  $P$  waveform recorded at a specific station may be used as  
 157 the reference. Considering the long aperture of the B-arrays (4-8 km; Fig. 2), we estimate  
 158 the  $P$ -wave delay time pattern by cross-correlating waveforms within a narrow  $P$ -wave  
 159 window (Fig. 3b) for every pair of stations  $i$  and  $j$ . The center of the narrow  $P$ -wave  
 160 window is determined based on the array-mean envelope function (Fig. 3b), and the peak  
 161 frequency of the array-mean  $P$ -wave amplitude spectrum (Fig. 3c) is used to set the  
 162 window width to be twice the dominant period. To further enhance the  $P$ -wave signals,  
 163 we apply another filter with a narrower frequency band (black dashed lines in Fig. 3c) to  
 164 the teleseismic data prior to the cross-correlation.

165 Let  $\tilde{t}_{ij}$  be the time delay corresponding to where the cross-correlation function  
 166 between  $P$  waveforms recorded at the  $i$ - and  $j$ -th stations reaches the maximum,

$$\tilde{t}_{ij} = \tilde{T}_i - \tilde{T}_j, \quad (1a)$$

167 where  $\tilde{T}_i$  and  $\tilde{T}_j$  are the teleseismic  $P$ -wave travel times at the  $i$ - and  $j$ -th stations,  
 168 respectively. Since the mean of the arrival time pattern  $\tilde{T}_i$  has no significance for our  
 169 imaging, we can ignore the constant  $\tilde{T}_j$  in equation (1a) and the delay time pattern is  
 170 given by  $\tilde{T}_{i_j} = \tilde{t}_{ij}$  when the  $j$ -th station is fixed and set to be the reference. We note that  
 171 the delay time patterns obtained by using different reference stations should be  
 172 consistent, i.e.,  $\tilde{T}_{i_{j_1}} - \tilde{T}_{i_{j_2}}$  is a constant. Thus, we can minimize the measurement error  
 173 by averaging equation (1a) over  $j$ ,

$$\tilde{T}_i = \sum_{j=1}^N \tilde{t}_{ij} / N + \sum_{j=1}^N \tilde{T}_j / N = \sum_{j=1}^N \tilde{t}_{ij} / N + C, \quad (1b)$$

174 where  $N$  is the number of stations and  $C$  is a constant. We again ignore the constant  $C$   
 175 and remove the effect of un-modeled topography from the teleseismic  $P$ -wave delay time

$$T_i = \sum_{j=1}^N \tilde{t}_{ij} / N - \Delta h_i / v_{\text{corr}}, \quad (2)$$

176 where  $v_{\text{corr}}$  is the  $P$ -wave velocity ( $V_p$ ) and  $\Delta h_i = h_i - \sum_{j=1}^N h_j / N$  represents the  
 177 relative topography, with  $h_i$  indicating the elevation at the  $i$ -th station (Figs. 2b-e). Here,  
 178 for the topographic correction, we assume a vertical-incidence angle for the incoming  $P$   
 179 wave and a constant  $V_p$  that is likely representative of velocity structures averaged over  
 180 the top 1-2 km (e.g., Park et al., 2019). Since the velocity structure at the shallow section  
 181 is poorly constrained by existing velocity models, we use two constant  $V_p$  values, 2 km/s  
 182 and 4 km/s, to estimate the lower and upper limits of  $v_{\text{corr}}$ .

183

### 184 3.1.2 Results

185 Coherent  $P$  arrivals, with different peak frequencies, are observed crossing the array  
 186 for the four events in Figure S1. Although the frequency content of the  $P$  waveforms is  
 187 different between events, the obtained arrival patterns prior to topographic correction are  
 188 in general consistent (e.g., higher velocity in the northeast beneath array B4 in Fig. 4d).  
 189 The black curves in Figure 4 depict the teleseismic  $P$ -arrival patterns for each array  
 190 averaged over all events with the standard deviation of the mean giving the uncertainty,  
 191 and the delay times after correcting the array topography are illustrated as colored dashed  
 192 curves. Features of delay-time patterns associated with a velocity contrast across the fault  
 193 (i.e., a smoothed step function as in Fig. 6d of Qiu et al., 2017) and a low-velocity zone  
 194 (i.e., a mountain-shaped function as in Fig. 6b of Qiu et al., 2017) are both observed in  
 195 the results after the topographic correction.

196 Delay-time patterns resolved at arrays B1 and B4 yield clear velocity contrasts across  
 197 the fault, with the southwest block having later arrivals indicating slower velocity ( $\sim 0.15$   
 198 s and  $\sim 0.25$  s in  $P$ -wave arrival time; Figs. 4a and 4d). Topographic corrections have  
 199 minor effects on the resolved arrival-time patterns at both arrays, as differences between  
 200 the two dashed curves are negligible in Figures 4a and 4d. Compared to the pattern  
 201 dominated by the velocity contrast, the time delay associated with low-velocity zones is  
 202 less obvious and comparable to the level of uncertainties (Figs. 4a and 4d). In contrast,



203 the dominant feature in arrival patterns resolved at arrays B2 and B3 yields several ~1-  
204 km-wide low-velocity zones that generate a maximum time delay of ~0.04 s (Figs. 4b-c):  
205 two centered at about 2.5 km southwest and 0.5 km northeast of the center of array B2;  
206 one centered at ~0.5 km southwest of the B3 array center.

207 Although the topographic correction has negligible effects on the low-velocity zones  
208 resolved at arrays B2 and B3, the time delays associated with velocity contrasts across  
209 the fault beneath the two arrays are much weaker and vary significantly with the  $V_p$  used  
210 in the correction (Figs. 4b-c). Different from the other three arrays, the polarity of the  
211 velocity contrast at array B3 is flipped for arrival patterns resolved using  $V_p$  of 2 km/s  
212 and 4 km/s. This is likely due to the combination of the larger difference in topography  
213 and smaller velocity contrast at arrays B2 and B3. Therefore, we do not discuss the  
214 velocity contrasts resolved from teleseismic  $P$  waves recorded at arrays B2 and B3 in  
215 later sections.

216

## 217 3.2 Local $P$ -wave delay time analysis

218  $P$  waves from local earthquakes recorded by the B-arrays are observed at higher  
219 frequencies (peaks at ~8 Hz; e.g., Fig. 5a) compared to those of teleseismic events  
220 (between 0.5-2 Hz; e.g., Fig. 3). Thus, higher resolution images of local fault zone  
221 structures can be achieved by analyzing arrival times of direct  $P$  waves from local  
222 earthquakes across each array.

223

### 224 3.2.1 Methodology

225 Compared with teleseismic arrivals, the effect of source-receiver geometry on  $P$   
226 waves for local earthquakes recorded by an array requires additional processing than the  
227 plane wave correction used in section 3.1.1. To extract the variations in  $P$ -wave arrival  
228 times associated with local fault-zone structures, we first suppress the contributions from  
229 source-receiver geometry and topographic variations by dividing the time axis of the  $P$   
230 waveform recorded at the  $i$ -th station for event  $j$  with its corresponding propagation  
231 distance  $H_{ij}$  (e.g., from Fig. 5a to 5b). Here, we use the hypocentral distance to  
232 approximate  $H_{ij}$ .  $P$ -wave picks,  $s_{ij} = t_{ij}/H_{ij}$  in units of slowness (e.g., Figs. 5b and S5b-  
233 S7b), are then picked via the short-term-average/long-term-average (STA/LTA)

234 algorithm (Allen, 1978) using waveforms within the slowness range of 0.15-0.25 s/km (to  
 235 exclude the effect of *S* waves). The *P*-wave SNR is calculated as the ratio between the  
 236 maximum and root mean square amplitudes of waveforms in slowness windows from  $s_{ij}$   
 237 to 0.25 s/km and 0.15 s/km to  $s_{ij}$ , respectively. *P*-wave picks with SNR less than 10 are  
 238 not used, and events are excluded if less than 80% of the array shows good quality *P*-  
 239 wave picks (SNR > 10).

240 The array-mean slowness  $\bar{s}_j = \sum_{i=1}^M s_{ij}/M$ , with  $M$  being the number of stations, can  
 241 vary significantly with focal depth and epicenter location (due to 3-D velocity structures).  
 242 Therefore, we use relative slowness,  $\hat{s}_{ij} = s_{ij}/\bar{s}_j$  (e.g., Qiu et al., 2017; Share et al.,  
 243 2017) to characterize statistical features of the local structure-related *P*-wave arrival  
 244 pattern using all available events. We can also estimate the local structure-related *P*-wave  
 245 arrival pattern in delay time,  $\delta t_{ij}$  for station  $i$  and event  $j$ , as  $\delta t_{ij} = (s_{ij} - \bar{s}_j) \cdot H_{ij}$ . Since  
 246 the existing velocity models indicate that structures in the Ridgecrest area are highly  
 247 heterogeneous, we only analyze *P* waves from events with depth > 5 km and close to  
 248 each array (red box in Figs. 5c and S5c-S7c) to ensure that the hypocentral distance is a  
 249 good approximation of the propagation distance  $H_{ij}$  and the resolved delay time pattern is  
 250 representative of local structures beneath the array.

251 Based on previous fault zone studies (e.g., Qiu et al., 2017; Share et al., 2017), the  
 252 observed *P*-wave travel time at station  $i$  for a near-fault event  $j$  mainly consists of two  
 253 components:

$$t_{ij} = s_{ij} \cdot H_{ij} \approx \bar{s}_j \cdot H_{ij} \cdot (1 + \eta_i) + \Delta t_{ij}. \quad (3)$$

254 The first term of equation (3) indicates the time delay associated with the cross-fault  
 255 velocity contrast beneath the array, and, ideally,  $\eta_i$  is a step function, i.e., equals  $-\eta/2$   
 256 and  $\eta/2$  ( $\eta < 1$ ) for stations on the faster and slower crustal blocks, respectively. The  
 257 second term  $\Delta t_{ij}$  represents the contribution of local structures beneath the array at  
 258 shallow depth (e.g., fault damage zone, sedimentary basin). Let  $\theta_j$  be the average incident  
 259 angle of *P* waves from event  $j$  to the array,  $\Delta t_{ij}$  is inversely proportional to  $\cos \theta_j$ , i.e.,  
 260  $\Delta t_{ij} \approx \tau_i / \cos \theta_j$ , where  $\tau_i$  is the delay time of a vertically incident *P* wave associated  
 261 with shallow structures beneath the array at station  $i$ .

262 Following the derivation in Text S1, the arrival patterns averaged over all near-fault  
 263 and close-to-array events are approximately given by:

$$\hat{S}_i = \sum_{j=1}^N \hat{s}_{ij} / N \approx 1 + \eta_i + \tau_i / (\tilde{t}_i \cos \tilde{\theta}) \approx 1 + \eta_i + \tau_i / (\bar{t} \cos \tilde{\theta}), \quad (4a)$$

264 in relative slowness, and

$$\delta T_i = \sum_{j=1}^N \delta t_{ij} / N \approx \eta_i \cdot \bar{t}_i + \tau_i / \cos \tilde{\theta} \approx \eta_i \cdot \bar{t} + \tau_i / \cos \tilde{\theta}, \quad (4b)$$

265 in delay time, after dropping the higher order terms.  $\tilde{t}_i$  and  $\bar{t}_i$  are the harmonic and  
 266 arithmetic means of  $P$ -wave travel time  $t_{ij}$ , respectively, over all events.  $N$  is the number  
 267 of events and  $\tilde{\theta}$  is the mean incidence angle averaged over all events.  $\bar{t}$  and  $\bar{t}$  denote the  
 268 array-mean travel times of  $\tilde{t}_i$  and  $\bar{t}_i$ , respectively. It is interesting to note that the shape of  
 269 arrival patterns  $\hat{S}_i$  and  $\delta T_i$  is the same, i.e.,  $\delta T_i / (\hat{S}_i - 1)$  is a constant, when  $\tilde{t} \approx \bar{t}$ .

270

### 271 3.2.2 Results

272 Figure 6a shows the results of statistical analysis on the local structure-related  $P$ -wave  
 273 arrival pattern in relative slowness ( $\hat{S}_i$  in eq. 4a) and delay time ( $\delta T_i$  in eq. 4b) for array  
 274 B1 using 189 near-fault events with depth  $> 5$  km outlined by the red box in Figure 5c.  
 275 The relative slowness patterns are averaged over all analyzed events and the standard  
 276 deviation of the mean is used to estimate the uncertainty. The small error bars and  
 277 confined width of histograms suggest that the mean relative slowness curve is  
 278 representative of the patterns observed from all analyzed events. The mean pattern in  
 279 delay time ( $\delta T_i$ ) with small uncertainties (Fig. 6a) is observed to have the same shape as  
 280 that of the relative slowness, i.e.,  $\delta T_i / (\hat{S}_i - 1)$  is approximately a constant. This is  
 281 consistent with equation (4) when  $\tilde{t} \approx \bar{t}$ .

282 Good agreement between the mean patterns of relative slowness and delay time with  
 283 small uncertainties is also observed at arrays B2-B4 in Figures 6c, 6e, and 6g. Consistent  
 284 with the teleseismic  $P$ -wave arrival time pattern shown in Figure 4, we observe the  
 285 features of delays in local  $P$ -wave arrival time associated with a step-function-like and  
 286 several mountain-shaped components at each array (left panels of Fig. 6) that likely  
 287 correspond to a velocity contrast across the fault and low-velocity zones, respectively.

288 Similar mean patterns of relative slowness are also observed for subsets of events  
 289 grouped according to different narrow ranges of depth (Figs. S8a-S11a). The polarity of  
 290 the velocity contrast is the same for arrays B1 and B4 (Figs. 6a and 6g), with the  
 291 southwest block being slower, consistent with results of the teleseismic delay time  
 292 analysis (Figs. 4a and 4d). However, delay time patterns at arrays B2 and B3 show the  
 293 opposite polarity (Figs. 6c and 6e), i.e., the northeast block having slower velocity. This  
 294 is consistent with results of the teleseismic delay time analysis before the topographic  
 295 correction (Figs. 4b-c).

296 We note that delay times associated with shallow materials ( $\tau_i$  in eq. 4a) could also  
 297 yield a step-function-like pattern (e.g., variations in sediment thickness across fault).  
 298 Thus, the amplitude of the step-function-like component,  $\tilde{\eta}$ , is an upper limit of the  
 299 magnitude of the cross-fault velocity contrast. We measure the amplitude of  $\tilde{\eta}$  as the  
 300 difference between relative slowness values averaged over stations on the southwest and  
 301 northeast edges of the array (left panels of Fig. 6), and the values are 5.3%, 0.8%, 3.9%,  
 302 and 8.8% at the sites of arrays B1-B4, respectively. Following equation (4a), if the  
 303 observed step-function-like pattern is due to variations in shallow materials, i.e.,  
 304  $\tau_i/(\tilde{t} \cos \tilde{\theta})$ , the amplitude of  $\tilde{\eta}$  should decrease with depth as the mean incidence angle  
 305  $\tilde{\theta}$  and travel time  $\tilde{t}$  increase with propagation distance. This contradicts the observations  
 306 that  $\tilde{\eta}$  increases with depth at array B2 (Fig. S9a) and only slightly varies with depth at  
 307 arrays B1 (Fig. S8a), B2 (Fig. S10a), and B4 (Fig. S11a), suggesting the observed step-  
 308 function-like pattern is likely a good approximation of the cross-fault velocity contrast, if  
 309 the contribution due to elevation variation is negligible.

310 To further analyze the effect of array topography in the step-function-like component  
 311  $\tilde{\eta}$ , we first model the delay times of cross-fault velocity contrast (i.e.,  $\eta_i \cdot \bar{t}$  in eq. 4b) with  
 312 a smoothed step function (Text S2). The modeled delay times of cross-fault velocity  
 313 contrast consist of three components: a linear trend within a transition zone between two  
 314 groups of stations at the southwest and northeast edges with constant values (eq. S5 in  
 315 Text S2; Fig. 6). We then illustrate the location of the resolved transition zone beneath  
 316 each array in Figure 2. At array B2, the span of the transition zone covers the area with a  
 317 steep slope in the array topography (Fig. 2c). Considering the large variation in elevation  
 318 ( $> 100$  m) and the small amplitude of  $\tilde{\eta}$  (0.8%), we conclude that the modeled cross-fault

319 velocity contrast may be dominated by the residual in topographic correction rather than  
 320 structure-related delay times. In contrast, for the other three arrays, the topography  
 321 variation is less significant and the amplitude of  $\tilde{\eta}$  is much larger ( $> 4\%$ ), indicating the  
 322 array topography likely has negligible contribution to the modeled cross-fault velocity  
 323 contrast.

324 The width of these transition zones and their locations relative to fault surface traces  
 325 provide additional information on the internal structures of the fault zone. At array B1,  
 326 the southwest edge of the transition zone correlates well with the surface trace of the Mw  
 327 7.1 earthquake (Fig. 2b), which is indicative of asymmetric rock damage offset to the  
 328 northeast (faster side). At array B3, the northeast edge of the transition zone agrees well  
 329 with the surface trace of the Mw 6.4 earthquake. The data recorded by array B3, crossing  
 330 the surface ruptures of both the Mw 6.4 and Mw 7.1 events, likely detect the velocity  
 331 contrast across the fault that hosted the Mw 6.4 earthquake, with the northwest side being  
 332 higher in velocity. An asymmetric rock damage offset to the faster side (northwest) is  
 333 also observed beneath array B3 (Fig. 2d). At array B4, the transition zone is much wider  
 334 and almost covers the entire array. This is consistent with the fact that the array is at the  
 335 southeast end of the Mw 7.1 earthquake rupture, where the rupture zone has several  
 336 surface traces and is less localized (Fig. 2e).

337 Low-velocity zones that further delay the  $P$ -wave arrivals are also observed at each  
 338 array, in addition to the pattern associated with the cross-fault velocity contrast (left  
 339 panels of Fig. 6). To highlight contributions from these low-velocity zones (i.e.,  
 340  $(\tau_i / (\tilde{\tau} \cos \tilde{\theta}))$  in eq. 4a), the right panels of Figure 6 show the mean delay time pattern by  
 341 subtracting the modeled  $\eta_i \cdot \bar{\tau}$  from  $\delta T_i$  (eq. 4b). A heat map of delay times  $\delta T_i$  after  
 342 subtracting the modeled  $\eta_i \cdot \bar{\tau}$  is also shown. Similar delay patterns of  $\tau_i$  reflecting  
 343 shallow materials beneath the array are seen using events within different narrow ranges  
 344 of depth (Figs. S8b-S11b). The range of delay patterns related to the major low-velocity  
 345 zones underneath each array are outlined with green dashed lines in Figure 6. The slower  
 346 inner cores (with peak delay time  $> 0.03$  s) of these low-velocity zones are marked by the  
 347 red dashed lines.

348 Consistent with the teleseismic  $P$ -wave arrival patterns obtained at arrays B2 and B3  
 349 (Figs. 4b-c), we observe low-velocity zones with comparable widths centered at the same

350 locations. In addition, we retrieve higher resolution images of the narrower and slower  
351 inner cores that correlate well with locations of the local peaks identified in the  
352 teleseismic  $P$ -wave delay time patterns (Figs. 4b-c). This is likely due to the shorter  
353 wavelength of local seismic  $P$  waves that can provide high-resolution images of internal  
354 fault-zone structures (e.g., Dahlen et al., 2000). Delay patterns related to low-velocity  
355 zones are also observed in the results for arrays B1 and B4 (Figs. 6b and 6h), which are  
356 hard to identify in the teleseismic delay time analyses (Figs. 4a and 4d) due to large  
357 uncertainties (i.e., insufficient number of analyzed events).

358 We note that consistent patterns of the cross-fault velocity contrast and low-velocity  
359 zones are observed (with different amplitudes) in results obtained using events with large  
360 along-fault distances (Figs. S8c-d, S9c-d, S10c-d, and S11c-d). To better visualize the  
361 locations of these major low-velocity zones with respect to the array configurations and  
362 fault surface traces, we depict the core and entire range of these zones in Figure 2. In  
363 general, locations of the identified low-velocity zones correlate well with surface traces  
364 of the 2019 Ridgecrest earthquake sequence (Fig. 2) inferred from Xu et al. (2020). This  
365 suggests that these low-velocity zones are likely indicative of fault damage zones or  
366 sedimentary basins around fault segments.

367

### 368 3.3 Fault-zone trapped waves

369 A low-velocity fault-damage zone that is sufficiently uniform over a given distance  
370 can act as a waveguide and generate, in addition to delay times and motion amplification,  
371 trapped waves resulting from constructive interference of critically reflected phases  
372 within the waveguide (e.g., Ben-Zion & Aki 1990; Igel et al., 1997; Jahnke et al., 2002).  
373 Such waves have been observed at many locations, including the San Jacinto fault zone  
374 (e.g., Lewis et al., 2005; Qin et al., 2018; Qiu et al., 2017; Share et al., 2019; Wang et al.,  
375 2019), the Parkfield section of the San Andreas fault (e.g., Li et al., 1990; Lewis and Ben-  
376 Zion, 2010; Ellsworth & Malin, 2011), and various other faults in California, Japan, Italy,  
377 Turkey, and other places. Catchings et al. (2016) used peak ground velocities of  $P$  and  $S$   
378 waveforms recorded by cross-fault linear arrays to infer the location and width of the  
379 West Napa-Franklin fault zone. Similarly, we find fault-damage-zone-related  
380 amplification in data recorded by the B-arrays (e.g., Figs. 7 and S12) and use such

381 amplification to detect FZTW candidates. In this section, we first infer the location and  
382 width of fault damage zones that produce FZTWs using waveforms for the fault-parallel  
383 component, and then use waveforms of these candidates recorded by array B4 to invert  
384 for properties (e.g., width, velocity, and attenuation) of the local fault-zone waveguide.

385

### 386 *3.3.1 Methodology*

387 Figure 7a shows *S* waveforms recorded on the fault-parallel component of array B4  
388 for an example event (Fig. 1). Following Ben-Zion et al. (2003) and Qiu et al. (2017, Fig.  
389 S6), several preprocessing steps are applied to the data prior to FZTW analyses. These  
390 include instrument response removal, integration to displacement seismogram, tapering  
391 between 1 s before and 2 s after the *S* pick, and convolution with  $1/t^{1/2}$  to convert a point-  
392 source response to that of an equivalent *SH* line dislocation source (e.g., Igel et al., 2002;  
393 Vidale et al., 1985). Compared to the raw recordings (Fig. S12), clearer Love-type  
394 waveform sections with large amplitudes and lower frequency are found at a group of  
395 stations (stations B416-423; Fig. 7a) in the southwest part of the array.

396 Figure 7b displays distributions of peak ground velocities (PGV) and root mean  
397 square amplitudes (RMS) of the fault-parallel-component *S* waveforms, normalized by  
398 the maximum value of the entire array. Large values of PGV and RMS are seen at  
399 stations with FZTW, with considerably higher amplitudes than at the rest of the array. We  
400 define the likelihood of a FZTW recorded by a station as the multiplication of PGV and  
401 RMS (Fig. 7b). The likelihood curve measured for each event is normalized by the  
402 maximum value of the entire array. After averaging the likelihood curves over all  
403 analyzed events, we highlight the array sections that have high likelihood of recording  
404 FZTWs (Fig. 8); these sections can be used to infer the location and width of fault-zone  
405 waveguides.

406 Since FZTWs are observed in *S* waveforms recorded at stations B416-B423 of array  
407 B4 for the example event in Figure 7a, we can also identify candidate events with similar  
408 good-quality FZTWs through template matching, i.e., cross-correlating the fault-parallel  
409 component *S* waveforms recorded by stations B416-B423 for each event with those of the  
410 example event. The trapped waves of candidate events (Fig. 9a) that yield cross-  
411 correlation coefficients higher than 0.85 (e.g., Fig. 9b) are averaged (Fig. 9c) and inverted

412 for properties (e.g., width, shear velocities, and attenuation) of the average fault-zone  
413 waveguide using a genetic inversion algorithm (e.g., Ben-Zion et al., 2003; Lewis et al.,  
414 2005; Qiu et al., 2017).

415 We test a total of 10,000 models (50 generations and 200 models per generation) to  
416 obtain a good estimate of the fault-zone parameters in the inversion. Parameters of the  
417 best-fitting model and the 2,000 models (investigated in the last 10 generations) are  
418 extracted from the inversion. Because there are strong trade-offs between model  
419 parameters governing FZTWs (e.g., Ben-Zion, 1998; Jahnke et al., 2002; Peng et al.  
420 2003), a successful inversion not only yields good waveform fits but also shows  
421 consistency between parameters of the best-fitting model and peaks of the probability  
422 density distributions of parameters developed in the last 10 generations. Additional  
423 details on the method can be found in section 3.4 of Qiu et al. (2017) and Ben-Zion et al.  
424 (2003).

425

### 426 *3.3.2 Results*

427 Figure 8 shows the distributions of FZTW likelihood values as a function of station  
428 location, estimated at arrays B1-B4 for all events within the red box shown in Figure 1.  
429 The likelihood values averaged over all analyzed events are representative of the in-situ  
430 amplification in *S*-wave. A good correlation is found in locations between local maxima  
431 of the likelihood curve and slower inner cores of the low-velocity zones identified from  
432 the local *P*-wave delay time analysis (Section 3.2; Fig. 8). This suggests that the observed  
433 inner cores of these low-velocity zones not only significantly delay the *P* arrivals but also  
434 amplify the incoming *S* waves.

435 However, not all stations within the inner cores of low-velocity zones identified in  
436 Figure 6 yield the same peak value of FZTW likelihood (Fig. 8). At array B4, the location  
437 of the candidate fault-zone waveguide (B417-B422; Figs. 7a and 8d) is in good  
438 agreement with the inner core of low-velocity zones that yields the highest likelihood  
439 value. We do not detect candidate FZTW at stations within the other low-velocity zones  
440 with much lower peak likelihood values. This is consistent with detailed fault-zone  
441 studies at Parkfield (Lewis & Ben-Zion, 2010), the rupture zone of the 1992 Landers  
442 earthquake (Peng et al., 2003), and fault zones in Japan (Mamada et al. 2004; Mizuno et



443 al. 2008). These studies showed that various sections of fault zones produce delay times  
444 and other signals of damaged rocks but are either too heterogeneous or have significant  
445 segmentation between sources and receivers to generate trapped waves (e.g., Igel et al.  
446 1997, 2002; Jahnke et al. 2002).

447 Not all analyzed events show *S*-wave amplification patterns that are consistent with  
448 the averaged curve. We first detect candidate events that show high FZTW likelihood  
449 values at stations B417-B422 (Fig. 8d) by cross-correlating the likelihood pattern  
450 measured for each event (e.g., black curve in Fig. 7b) with that of the mean (e.g., red  
451 curve in Fig. 8d). More than 600 events with cross-correlation coefficients higher than  
452 0.95 are identified as FZTW candidates. We further select 33 events (Fig. 9a) that  
453 produce high-quality FZTWs (e.g., Fig. 9b) from the candidate events, through template  
454 matching of fault-parallel component *S* waveforms at stations B416-B423 (using FZTWs  
455 shown in Fig. 7a as the template; Section 3.3.1). These high-quality FZTW candidates  
456 show a consistent source-receiver path (top inset of Fig. 9a), indicating the depth of the  
457 fault-zone waveguide is likely shallower than 5 km, and there is an optimal range of  
458 incidence angle for injecting seismic energy into the fault damage zone beneath array B4  
459 (e.g., Fohrmann et al. 2004).

460 Compared to FZTW observed from each candidate event (e.g., Fig. 9b), the stacked  
461 recordings (Fig. 9c) yield much higher SNRs and can thus provide more reliable and  
462 robust estimations of the average fault-zone waveguide properties. Figure 10 presents the  
463 inversion results from modeling the stacked waveforms shown in Figure 9c (in red). The  
464 best-fitting model yields good waveform fits (Fig. 10a) and suggests a simplified (i.e.,  
465 vertical rectangular-shaped) fault-zone waveguide with a width of  $\sim 280$  m, *Q* value of  
466  $\sim 30$ , and *S*-wave velocity  $\sim 80\%$  of the surrounding host rocks (Fig. 10b). The estimated  
467 propagation distance inside the waveguide is  $\sim 5.4$  km (Fig. 10b). Because this includes a  
468 propagation component along-strike (i.e., non-vertical incidence angle), it suggests a  
469 waveguide depth of  $\sim 4$  km ( $= 5.4/\sqrt{2}$ ). The estimated average *S*-wave velocity in the  
470 host rock is  $\sim 4.1$  km/s, with the northeast block being  $\sim 4.2\%$  faster, consistent with  
471 results from the *P*-wave delay time analysis at array B4 ( $\sim 3\%$  velocity contrast across  
472 LVZ#5 with higher velocity in the northeast; Fig. 6g). The parameters of fault-zone  
473 models from the last 10 generations (2,000 models) are shown in Figure 10b, along with

474 the corresponding probability density functions computed as the frequency of each  
475 parameter value weighted by the fitness values (Ben-Zion et al., 2003). The good  
476 waveform fits, combined with the consistency between best fitting parameters and peaks  
477 of the probability density functions (Fig. 10b), suggest that the best-fitting model  
478 parameters provide robust estimates of the average properties of the fault-zone  
479 waveguide.

480 In addition to FZTWs, we detect in data of stations B420 and B422 (Fig. S13) clear  
481 fault-zone head waves (FZHWs) that refract along a bimaterial fault interface (e.g., Ben-  
482 Zion, 1990) and arrive  $\sim 0.1$  s earlier than the direct  $P$ -wave. The early-arriving FZHWs  
483 are inferred from horizontal particle motion analysis modified from the method of Bulut  
484 et al. (2012). It is important to note that in the polarization analysis we only focus on the  
485 rotation of the horizontal particle motion between FZHW and direct  $P$ -wave. This is  
486 because the polarization direction of horizontal particle motion for the direct  $P$  wave at  
487 stations inside a damage zone (Fig. S13) can deviate significantly from the source-  
488 receiver back azimuth. Since the differential time between the FZHW and direct  $P$ -wave  
489 decreases significantly from the northeast (B422) to the southwest (B420) over a short  
490 distance ( $\sim 0.1$  km), the observed FZHW is likely traveling along a local interface that is  
491 associated with the edge of the damage zone (e.g., Qiu et al., 2017) on the northeast side  
492 between stations B422 and B423. Similar FZTW and FZHW signals are also clearly  
493 observed in the data of array B2 (e.g., Fig. S14) but not for arrays B1 and B3.

494

#### 495 **4. Discussion**

496 We analyze systematically time delays of  $P$  arrivals from teleseismic and local  
497 earthquakes,  $S$ -wave amplification, and fault zone trapped waves in data recorded by four  
498 long-aperture (4-8 km) arrays at different locations along the rupture zone of the 2019  
499 Mw 7.1 Ridgecrest earthquake (Fig. 2). The analyses allow us to derive information on  
500 velocity contrast interfaces and low velocity damage zones at scales of  $\sim 100$  m associated  
501 with the Ridgecrest rupture zone. The results are complementary to tomographic velocity  
502 models that provide a regional context but do not resolve the internal structural elements  
503 of the Ridgecrest rupture zone imaged in this work.

504 The delay times of  $P$ -waves from both teleseismic and local earthquakes, after proper  
 505 corrections for propagation and topography effects, show clear and consistent velocity  
 506 contrasts across the rupture zone, with a higher velocity in the northeast at arrays B1  
 507 (Figs. 4a and 6a) and B4 (Figs. 4d and 6g). Combining the delay times inferred from  
 508 teleseismic  $P$  waves in Figure 4 and the amplitudes of cross-fault velocity contrast in the  
 509 left panels of Figure 6, we can estimate the depth extent of the contrast interface beneath  
 510 each array. For a constant velocity contrast across the fault with an amplitude of  $\eta$   
 511 extending to a depth of  $H_c$ , the time delay between teleseismic  $P$  arrivals, assuming a  
 512 vertical angle of incidence, at stations on different sides of the fault is given by

$$\Delta t \approx \eta \cdot H_c / \bar{V}_p, \quad (5)$$

513 where  $\bar{V}_p$  is the average  $P$ -wave velocity of the upper crust. We set  $\bar{V}_p = 5.6$  km/s as  
 514 inferred from the mean of the average slowness  $\bar{s}_j$  (eq. 3) over all event-array pairs. The  
 515  $H_c$  beneath arrays B1 ( $\Delta t = 0.15$  s from Fig. 4a and  $\eta = 5.3\%$  from Fig. 6a) and B4  
 516 ( $\Delta t = 0.25$  s from Fig. 4d and  $\eta = 8.8\%$  from Fig. 6g), computed using equation (5), are  
 517 both  $\sim 16$  km, suggesting a deep fault interface that likely extends to the seismogenic  
 518 depth (10-12 km) after taking measurement uncertainties (Figs. 4a and 4d) and non-  
 519 vertical angle of incidence into account.

520 We do not estimate the depth  $H_c$  for arrays B2 and B3 as the teleseismic  $P$ -wave  
 521 delay times  $\Delta t$  are highly dependent on the topographic correction (Section 3.1.2; Figs.  
 522 4b-c). The cross-fault velocity contrast observed in local  $P$ -wave delay time patterns  
 523 resolved at arrays B2 and B3 (Figs. 6c and 6e) suggests a higher velocity in the  
 524 southwest, the opposite of the polarity obtained at arrays B1 and B4 (Figs. 6a and 6g).  
 525 Further analysis of the transition zones (Figs. 2b-e) resolved from the modeled cross-fault  
 526 velocity contrasts (left panels of Fig. 6) indicates that: the observed velocity contrast  
 527 beneath array B2 is likely an artifact due to insufficient topographic correction; array B3  
 528 may detect the velocity contrast across the rupture zone of the Mw 6.4 earthquake; and  
 529 the broader transition zone beneath array B4 suggests the fault zone at the southeast edge  
 530 of the Mw 7.1 earthquake rupture is likely not as well localized (e.g., several rupture  
 531 surface traces; Fig. 2) as those beneath the other three arrays.

532 Symmetry properties of fault damage zones with respect to the main slip surface can  
533 provide information on the direction of earthquake ruptures (e.g., Ben-Zion & Shi, 2005;  
534 Dor et al., 2006; Mitchell et al., 2011; Xu et al., 2012). Statistically preferred rupture  
535 direction is expected for prominent bimaterial faults (e.g., Ampuero & Ben-Zion, 2008;  
536 Andrews and Ben-Zion, 1997; Shlomai & Fineberg, 2016; Weertman, 1980). However, a  
537 prominent large-scale velocity contrast is not expected across the Ridgecrest rupture zone  
538 based on the regional velocity models (Lee et al., 2014; Shaw et al., 2015; White et al.,  
539 2020) and total offset across the structure. The transition zones of the cross-fault velocity  
540 contrast resolved at arrays B1 (Fig. 2b) and B3 (Fig. 2d) are asymmetrically distributed to  
541 the faster side of the fault surface trace, which is likely indicative of asymmetric rock  
542 damage offset to the faster side of the rupture zone for the Mw 7.1 and Mw 6.4  
543 earthquakes, respectively. Since the transition zones resolved at arrays B2 and B4 are not  
544 well resolved, we do not discuss results obtained at these two locations (Figs. 2c and 2e).

545 Good agreement between locations of slower inner cores of the low-velocity zones  
546 identified from delay time analyses and the group of stations with amplified *S* waveforms  
547 (Fig. 8) is found beneath all four arrays. Combined with the narrow width (300-400 m;  
548 right panels of Fig. 6) of the inner cores, these zones that both significantly delay the *P*  
549 arrivals and amplify the incoming *S* waveforms are likely representative of localized  
550 damage zones, rather than variations in sedimentary thickness that usually yield much  
551 wider patterns of *S*-wave amplification. Waveform modeling of FZTWs detected at array  
552 B4 yields good waveform fits and an average waveguide with fault-zone parameters  
553 comparable to those inferred from previous studies in the SJFZ (Qin et al., 2018; Qiu et  
554 al., 2017; Share et al., 2017, 2019): width of ~300 m, *Q* of ~30, *S*-wave velocity  
555 reduction of ~20% inside the damage zone, and depth extent of 3-5 km (Fig. 10).

556 To further investigate the structures that produce the observed low-velocity zones, we  
557 map the inner core and entire span of these zones together with locations of fault surface  
558 traces (or their extrapolations) and the surface geology compiled by the USGS in Figure  
559 2. The low-velocity zone (LVZ#1 in Fig. 6b) identified at array B1, in contrast to the  
560 resolved transition zone (Fig. 2b), is on the southwest (slower) side of the surface trace of  
561 the main rupture zone. There are two well-separated inner cores (Fig. 2b) that yield both  
562 large delay times (Fig. 6b) and *S*-wave amplitudes (Fig. 8a). The inner core in the

563 southwest (Fig. 2b) is likely associated with the damage zone of past earthquake ruptures,  
564 since it is centered on a surface displacement mapped before the 2019 Ridgecrest  
565 earthquake. The northeast inner core (Fig. 2b), however, is likely representative of the  
566 damage zone of the Mw 7.1 Ridgecrest earthquake ruptures, as it is centered on the main  
567 rupture zone.

568 At array B2, two low-velocity zones (LVZ #2 and #3) are identified from Figures 6d.  
569 Different from the other three arrays, the surface geology beneath array B2 consists of  
570 two different types of rocks (alternating playa and igneous rocks; Fig. 2c), which likely  
571 explains the weak cross-fault velocity contrast resolved at this location (Figs. 4b and 6c).  
572 Both low-velocity zones are centered on the surface traces (or their extrapolations) of the  
573 main rupture zone, with the slower inner cores close to the fault traces. Good agreement  
574 between locations of low-velocity zones and surface traces of the 2019 Ridgecrest  
575 earthquake ruptures is also observed beneath arrays B3 (Fig. 2d) and B4 (Fig. 2e). Since  
576 the locations of these low-velocity zones correlate well with the fault surface traces rather  
577 than the surface geology, we conclude that: these low-velocity zones with slower inner  
578 cores that considerably amplify *S* waveforms depict the fault damage zones of the Mw  
579 7.1 earthquake rupture at arrays B2 and B4, and ruptures of both the Mw 6.4 and Mw 7.1  
580 earthquakes at array B3.

581 It is interesting to note that we find a clear and coherent secondary phase between *P*  
582 and *S* arrivals in waveforms recorded by part of array B4 for more than 10 events located  
583 beneath the array. Figure S15b shows such signals for an example event (circle in Fig.  
584 S15a). The strong phases are visible at stations B423-B457 (blue curve in Fig. S15b) and  
585 correlate well with the shape of the direct *P*-wave but with the opposite first-motion  
586 polarity (e.g., Fig. S15d) suggesting the signals are likely reflected or converted waves.  
587 Since the array-mean travel time of the direct *P*-wave is between 1-1.5 s, based on the  
588 ~0.5 s differential time between the direct *P* and the strong secondary waves (e.g., black  
589 and blue dashed lines in Fig. S15d), the reflection or conversion interface should be a few  
590 kilometers away from the array and is thus likely associated with the Garlock fault in the  
591 south rather than the rupture zone of the Mw 7.1 Ridgecrest earthquake (Fig. S15a).  
592 Detailed analysis of these candidate reflected/converted phases may require more  
593 sophisticated techniques, such as seismic migration of the arrival times and waveform

594 simulation with accurate source information (e.g., focal mechanism) for the  
595 understanding of the wave amplitudes. As these secondary signals detected in Figure S15  
596 are outside the scope of this paper, additional analysis of these phases will be the subject  
597 of a follow-up study.

598

## 599 **5. Conclusions**

600 The rupture zone of the Mw 7.1 Ridgecrest earthquake is shown to have seismic  
601 velocity contrast interfaces and damage structures with significant along-strike variations  
602 of local damage zones. The results are in overall agreement with and complementary to  
603 the mapped fault surface traces in the region (e.g., Xu et al., 2020) and previous analyses  
604 of aftershocks in the Ridgecrest sequence (e.g., Ross et al., 2019; Cheng & Ben-Zion,  
605 2020).

606 Delay times of *P* waves from teleseismic and local earthquakes recorded by arrays B1  
607 and B4 resolve velocity contrasts ranging from 5%-9% in  $V_p$  across the Ridgecrest  
608 rupture zone, which extend to a depth of  $\sim 16$  km, with the northeast being locally faster.  
609 Data recorded by array B3, crossing the surface ruptures of both the Mw 6.4 and Mw 7.1  
610 events, likely detects a  $\sim 4\%$  velocity contrast in  $V_p$  across the fault that hosted the Mw  
611 6.4 earthquake, with the northwest side having higher velocity. Asymmetric rock damage  
612 concentrated on the stiffer side of the fault is seen beneath arrays B1 and B3.

613 Low-velocity zones that further delay the *P* waves of local seismic events are  
614 centered on mapped surface traces of faults associated with both past and the 2019  
615 Ridgecrest earthquake ruptures. Considerable amplification is seen consistently in *S*  
616 waveforms recorded at stations within the slower inner core of the identified LVZ. Clear  
617 FZTWs are identified at arrays B2 and B4, and inversion of high-quality FZTWs at array  
618 B4 indicates a waveguide with average properties comparable to those found in previous  
619 studies at sites of the San Jacinto fault zone. Phases identified as FZHWS, associated with  
620 the northeast boundary of the fault zone waveguide, are observed at arrays B2 and B4.  
621 Coherent candidate reflected or converted waves are observed in data recorded at array  
622 B4. Additional analysis of these phases can provide additional constraints on prominent  
623 impedance interfaces associated with the Garlock fault and/or the Ridgecrest rupture  
624 zone.

625

626 **Data Availability**

627 The digital data are available in mseed day volume format, with each component in a  
628 separate volume. The data samples are 4 byte floats and consistently sampled at 500  
629 samples/second. Data described in this report are available from the IRIS Data  
630 Management Center (<https://ds.iris.edu/ds/nodes/dmc/data/>). An accompanying report for  
631 data acquisition is available from Catchings et al. (2020). Surface traces of the 2019  
632 Ridgecrest earthquake sequence shown in this study were determined by Xu et al. (2020).  
633 The geologic data depicted as the background of Figure 2 were obtained from the USGS  
634 website (<https://mrdata.usgs.gov/geology/state/state.php?state=CA>).

635

636 **Acknowledgements**

637 The rapid seismic deployment of nodes for the 2019 Ridgecrest earthquake sequence was  
638 partially supported by the U.S. Geological Survey, the Southern California Earthquake  
639 Center, and the National Science Foundation (grant EAR-1945781). Personnel from the  
640 USGS, University of California - Santa Barbara, University of Utah, University of  
641 Southern California, and the Naval Air Weapons Station (NAWS) – China Lake,  
642 including Elizabeth Berg, Joanne Chan, Coyn Criley, Garet Huddleston, Daniel  
643 Langermann Zhenning Ma, Andrew Madsen, Adrian McEvelly, Daniel Mongovin, and  
644 Jordan Wang, were invaluable in the rapid response. We thank IRIS-PASSCAL for  
645 providing 162 Fairfield Zland 3C nodes and Sandia National Laboratory for providing 54  
646 Fairfield 3C nodes, and the USGS for providing 245 SmartSolo 3C nodes. We thank  
647 Josh Bain, Stephan Bork, Kyle Buck, Darrin Clodt, John Foster, Allen Grossardt, Cyndy  
648 Hopkins, Hugh Jones, T.J. Larson, James Lovern, Sean Oleary, Nancy Pahr, Mike Pierce,  
649 Jacob Rivera, Vince Wallace, and Shane Williams of the NAWS-China Lake for access  
650 and field assistance. We thank Kate Scharer for coordination assistance with the NAWS.  
651 The manuscript benefits from useful comments by two anonymous reviewers, an  
652 anonymous Associate Editor and Editor Rachel Abercrombie. The research done in this  
653 paper was supported by the National Science Foundation (Award EAR-1945781), the  
654 U.S. Department of Energy (Award #DE-SC0016520), and the Southern California

655 Earthquake Center (based on NSF Cooperative Agreement EAR-1600087 and USGS  
656 Cooperative Agreement G17AC00047).

657

## 658 **References**

- 659 Aki, K. (1979). Characterization of barriers on an earthquake fault. *Journal of*  
660 *Geophysical Research*. <https://doi.org/10.1029/JB084iB11p06140>
- 661 Allen, R. (1978). Automatic earthquake recognition and timing from signal traces.  
662 *Bulletin of the Seismological Society of America*. 68 (5):1521-1532.
- 663 Ampuero, J. P., & Ben-Zion, Y. (2008). Cracks, pulses and macroscopic asymmetry of  
664 dynamic rupture on a bimaterial interface with velocity-weakening friction.  
665 *Geophysical Journal International*, 173(2), 674–692. [https://doi.org/10.1111/j.1365-](https://doi.org/10.1111/j.1365-246X.2008.03736.x)  
666 [246X.2008.03736.x](https://doi.org/10.1111/j.1365-246X.2008.03736.x)
- 667 Andrews, D. J., & Ben-Zion, Y. (1997). Wrinkle-like slip pulse on a fault between  
668 different materials. *Journal of Geophysical Research B: Solid Earth*.  
669 <https://doi.org/10.1029/96jb02856>
- 670 Ben-Zion, Y. (1990). The response of two half spaces to point dislocations at the material  
671 interface, *Geophys. J. Int.*, 101, 507-528.
- 672 Ben-Zion, Y. (1998). Properties of seismic fault zone waves and their utility for imaging  
673 low-velocity structures. *Journal of Geophysical Research: Solid Earth*.  
674 <https://doi.org/10.1029/98jb00768>
- 675 Ben-Zion, Y., & Aki, K. (1990). Seismic radiation from an SH line source in a laterally  
676 heterogeneous planar fault zone. *Bulletin - Seismological Society of America*.
- 677 Ben-Zion, Y., & Huang, Y. (2002). Dynamic rupture on an interface between a compliant  
678 fault zone layer and a stiffer surrounding solid. *Journal of Geophysical Research*.  
679 <https://doi.org/10.1029/2001jb000254>
- 680 Ben-Zion, Y., & Shi, Z. (2005). Dynamic rupture on a material interface with  
681 spontaneous generation of plastic strain in the bulk. *Earth and Planetary Science*  
682 *Letters*. <https://doi.org/10.1016/j.epsl.2005.03.025>
- 683 Ben-Zion, Y., Peng, Z., Okaya, D., Seeber, L., Armbruster, J. G., Ozer, N., et al. (2003).  
684 A shallow fault-zone structure illuminated by trapped waves in the Karadere-Duzce  
685 branch of the North Anatolian Fault, western Turkey. *Geophysical Journal*  
686 *International*. <https://doi.org/10.1046/j.1365-246X.2003.01870.x>
- 687 Brietzke, G. B., & Ben-Zion, Y. (2006). Examining tendencies of in-plane rupture to  
688 migrate to material interfaces. *Geophysical Journal International*.  
689 <https://doi.org/10.1111/j.1365-246X.2006.03137.x>
- 690 Bulut, F., Ben-Zion, Y., & Bohnhoff, M. (2012). Evidence for a bimaterial interface  
691 along the Mudurnu segment of the North Anatolian Fault Zone from polarization  
692 analysis of P waves. *Earth and Planetary Science Letters*.  
693 <https://doi.org/10.1016/j.epsl.2012.02.001>
- 694 Catchings, R. D., Goldman, M. R., Li, Y. G., & Chan, J. H. (2016). Continuity of the  
695 west napa-franklin fault zone inferred from guided waves generated by earthquakes  
696 following the 24 august 2014 Mw 6.0 south napa earthquake. *Bulletin of the*  
697 *Seismological Society of America*. <https://doi.org/10.1785/0120160154>
- 698 Catchings, R. D., M.R. Goldman, J.H. Steidl, J.H. Chan, A.A. Allam, C.J. Criley, Z. Ma,



- 699 D.S. Langermann, G.J. Huddleston, A.T. McEvilly, D.D. Mongovin, E.M. Berg, and  
700 Y. Ben-Zion, 2020. Nodal Seismograph Recordings of the 2019 Ridgecrest  
701 Earthquake Sequence, *Seism. Res. Lett.*, doi: 10.1785/0220200203.
- 702 Chen, K., Avouac, J. P., Aati, S., Milliner, C., Zheng, F., & Shi, C. (2020). Cascading  
703 and pulse-like ruptures during the 2019 Ridgecrest earthquakes in the Eastern  
704 California Shear Zone. *Nature Communications*, 11(1), 3–10.  
705 <https://doi.org/10.1038/s41467-019-13750-w>
- 706 Cheng, Y. and Y. Ben-Zion, 2020. Variations of earthquake properties before, during and  
707 after the 2019 M7.1 Ridgecrest, CA, earthquake, *Geophys., Res., Lett.*, 47,  
708 e2020GL089650, doi: 10.1029/2020GL089650.
- 709 Cochran, E., Li, Y. G., Shearer, P. M., Barbot, S., Fialko, Y., & Vidale, J. E. (2009).  
710 Seismic and geodetic evidence for extensive, long-lived fault damage zones.  
711 *Geology*. <https://doi.org/10.1130/G25306A.1>
- 712 Crotwell, H. P., Owens, T. J., & Ritsema, J. (1999). The TauP Toolkit: Flexible Seismic  
713 Travel-time and Ray-path Utilities. *Seismological Research Letters*.  
714 <https://doi.org/10.1785/gssrl.70.2.154>
- 715 Dahlen, F. A., Hung, S.-H., & Nolet, G. (2000). Frechet kernels for finite-frequency  
716 traveltimes - I. Theory. *Geophysical Journal International*, (141), 157–174.  
717 <https://doi.org/10.1007/978-3-319-06540-3>
- 718 Dor, O., Rockwell, T. K., & Ben-Zion, Y. (2006). Geological observations of damage  
719 asymmetry in the structure of the San Jacinto, San Andreas and Punchbowl faults in  
720 Southern California: A possible indicator for preferred rupture propagation  
721 direction. *Pure and Applied Geophysics*. <https://doi.org/10.1007/s00024-005-0023-9>
- 722 Ellsworth, W. L., & Malin, P. E. (2011). Deep rock damage in the san andreas fault  
723 revealed by P- and S-type fault-zone-guided waves. *Geological Society Special  
724 Publication*. <https://doi.org/10.1144/SP359.3>
- 725 Fohrmann, M., Igel, H., Jahnke, G., & Ben-Zion, Y. (2004). Guided waves from sources  
726 outside faults: An indication for shallow fault zone structure? *Pure and Applied  
727 Geophysics*. <https://doi.org/10.1007/s00024-004-2553-y>
- 728 Hauksson, E., Yang, W., & Shearer, P. M. (2012). Waveform relocated earthquake  
729 catalog for Southern California (1981 to June 2011). *Bulletin of the Seismological  
730 Society of America*. <https://doi.org/10.1785/0120120010>
- 731 Huang, Y., Ampuero, J. P., & Helmberger, D. V. (2014). Earthquake ruptures modulated  
732 by waves in damaged fault zones. *Journal of Geophysical Research: Solid Earth*.  
733 <https://doi.org/10.1002/2013JB010724>
- 734 Igel, H., Ben-Zion, Y., & Leary, P. C. (1997). Simulation of SH- and P-SV-wave  
735 propagation in fault zones. *Geophysical Journal International*.  
736 <https://doi.org/10.1111/j.1365-246X.1997.tb05316.x>
- 737 Igel, H., Jahnke, G., & Ben-Zion, Y. (2002). Numerical simulation of fault zone guided  
738 waves: Accuracy and 3-D effects. *Pure and Applied Geophysics*.  
739 <https://doi.org/10.1007/s00024-002-8724-9>
- 740 Jahnke, G., Igel, H., & Ben-Zion, Y. (2002). Three-dimensional calculations of fault-  
741 zone-guided waves in various irregular structures. *Geophysical Journal  
742 International*. <https://doi.org/10.1046/j.1365-246X.2002.01784.x>
- 743 Jia, Z., Wang, X., & Zhan, Z. (2020). Multifault models of the 2019 Ridgecrest sequence  
744 highlight complementary slip and fault junction instability. *Geophysical Research*

- 745 *Letters*. <https://doi.org/10.1029/2020GL089802>
- 746 Kennett, B. L. N., & Engdahl, E. R. (1991). Traveltimes for global earthquake location  
747 and phase identification. *Geophysical Journal International*.  
748 <https://doi.org/10.1111/j.1365-246X.1991.tb06724.x>
- 749 King, G. C. P. (1986). Speculations on the geometry of the initiation and termination  
750 processes of earthquake rupture and its relation to morphology and geological  
751 structure. *Pure and Applied Geophysics*. <https://doi.org/10.1007/BF00877216>
- 752 Kurzon, I., Vernon, F. L., Ben-Zion, Y., & Atkinson, G. (2014). Ground Motion  
753 Prediction Equations in the San Jacinto Fault Zone: Significant Effects of Rupture  
754 Directivity and Fault Zone Amplification. *Pure and Applied Geophysics*.  
755 <https://doi.org/10.1007/s00024-014-0855-2>
- 756 Lee, E.-J., Chen, P., Jordan, T. H., Maechling, P. B., Denolle, M. A., & Beroza, G. C.  
757 (2014). Full-3-D tomography for crustal structure in Southern California based on  
758 the scattering-integral and the adjoint-wavefield methods. *Journal of Geophysical*  
759 *Research: Solid Earth*. <https://doi.org/10.1002/2014JB011346>
- 760 Lewis, M. A., & Ben-Zion, Y. (2010). Diversity of fault zone damage and trapping  
761 structures in the Parkfield section of the San Andreas Fault from comprehensive  
762 analysis of near fault seismograms. *Geophysical Journal International*.  
763 <https://doi.org/10.1111/j.1365-246X.2010.04816.x>
- 764 Lewis, M. A., Peng, Z., Ben-Zion, Y., & Vernon, F. L. (2005). Shallow seismic trapping  
765 structure in the San Jacinto fault zone near Anza, California. *Geophysical Journal*  
766 *International*. <https://doi.org/10.1111/j.1365-246X.2005.02684.x>
- 767 Li, Y. G., Leary, P., Aki, K., & Malin, P. (1990). Seismic trapped modes in the Oroville  
768 and San Andreas fault zones. *Science*. <https://doi.org/10.1126/science.249.4970.763>
- 769 Li, Y. G., Aki, K., Adams, D., Hasemi, A., & Lee, W. H. K. (1994). Seismic guided  
770 waves trapped in the fault zone of the Landers, California, earthquake of 1992.  
771 *Journal of Geophysical Research*. <https://doi.org/10.1029/94jb00464>
- 772 Mamada, Y., Kuwahara, Y., Ito, H., & Takenaka, H. (2004). Discontinuity of the  
773 Mozumi-Sukenobu fault low-velocity zone, central Japan, inferred from 3-D finite-  
774 difference simulation of fault zone waves excited by explosive sources.  
775 *Tectonophysics*. <https://doi.org/10.1016/j.tecto.2003.09.008>
- 776 Mitchell, T. M., Ben-Zion, Y., & Shimamoto, T. (2011). Pulverized fault rocks and  
777 damage asymmetry along the Arima-Takatsuki Tectonic Line, Japan. *Earth and*  
778 *Planetary Science Letters*. <https://doi.org/10.1016/j.epsl.2011.04.023>
- 779 Mizuno, T., Kuwahara, Y., Ito, H., & Nishigami, K. (2008). Spatial variations in fault-  
780 zone structure along the Nojima fault, central Japan, as inferred from borehole  
781 observations of fault-zone trapped waves. *Bulletin of the Seismological Society of*  
782 *America*. <https://doi.org/10.1785/0120060247>
- 783 Ozakin, Y., Ben-Zion, Y., Aktar, M., Karabulut, H., & Peng, Z. (2012). Velocity contrast  
784 across the 1944 rupture zone of the North Anatolian fault east of Ismetpasa from  
785 analysis of teleseismic arrivals. *Geophysical Research Letters*.  
786 <https://doi.org/10.1029/2012GL051426>
- 787 Park, S., Tsai, V. C., & Ishii, M. (2019). Frequency-Dependent P Wave Polarization and  
788 Its Subwavelength Near-Surface Depth Sensitivity. *Geophysical Research Letters*.  
789 <https://doi.org/10.1029/2019GL084892>
- 790 Peng, Z., Ben-Zion, Y., Michael, A. J., & Zhu, L. (2003). Quantitative analysis of seismic

- 791 fault zone waves in the rupture zone of the 1992 Landers, California, earthquake:  
792 Evidence for a shallow trapping structure. *Geophysical Journal International*.  
793 <https://doi.org/10.1111/j.1365-246X.2003.02109.x>
- 794 Qin, L., Ben-Zion, Y., Qiu, H., Share, P. E., Ross, Z. E., & Vernon, F. L. (2018). Internal  
795 structure of the San Jacinto fault zone in the trifurcation area southeast of Anza,  
796 California, from data of dense seismic arrays. *Geophysical Journal International*,  
797 *213*(1), 98–114. <https://doi.org/10.1093/gji/ggx540>
- 798 Qiu, H., Ben-Zion, Y., Ross, Z. E., Share, P. E., & Vernon, F. L. (2017). Internal  
799 structure of the San Jacinto fault zone at Jackass Flat from data recorded by a dense  
800 linear array. *Geophysical Journal International*, *209*(3), 1369–1388.  
801 <https://doi.org/10.1093/gji/ggx096>
- 802 Ross, Z. E., Idini, B., Jia, Z., Stephenson, O. L., Zhong, M., Wang, X., et al. (2019).  
803 Hierarchical interlocked orthogonal faulting in the 2019 Ridgecrest earthquake  
804 sequence. *Science*. <https://doi.org/10.1126/science.aaz0109>
- 805 Rovelli, A., Caserta, A., Marra, F., & Ruggiero, V. (2002). Can seismic waves be trapped  
806 inside an inactive fault zone? The case study of Nocera Umbra, Central Italy.  
807 *Bulletin of the Seismological Society of America*.  
808 <https://doi.org/10.1785/0120010288>
- 809 Share, P. E., Ben-Zion, Y., Ross, Z. E., Qiu, H., & Vernon, F. L. (2017). Internal  
810 structure of the San Jacinto fault zone at Blackburn Saddle from seismic data of a  
811 linear array. *Geophysical Journal International*, *210*(2), 819–832.  
812 <https://doi.org/10.1093/gji/ggx191>
- 813 Share, P. E., Allam, A. A., Ben-Zion, Y., Lin, F.-C., & Vernon, F. L. (2019). Structural  
814 Properties of the San Jacinto Fault Zone at Blackburn Saddle from Seismic Data of a  
815 Dense Linear Array. *Pure and Applied Geophysics*, *176*(3), 1169–1191.  
816 <https://doi.org/10.1007/s00024-018-1988-5>
- 817 Shaw, J. H., Plesch, A., Tape, C., Suess, M. P., Jordan, T. H., Ely, G., et al. (2015).  
818 Unified Structural Representation of the southern California crust and upper mantle.  
819 *Earth and Planetary Science Letters*. <https://doi.org/10.1016/j.epsl.2015.01.016>
- 820 Shlomai, H., & Fineberg, J. (2016). The structure of slip-pulses and supershear ruptures  
821 driving slip in bimaterial friction. *Nature Communications*.  
822 <https://doi.org/10.1038/ncomms11787>
- 823 Spudich, P., & Olsen, K. B. (2001). Fault zone amplified waves as a possible seismic  
824 hazard along the Calaveras fault in central California. *Geophysical Research Letters*.  
825 <https://doi.org/10.1029/2000GL011902>
- 826 Thakur, P., Huang, Y., & Kaneko, Y. (2020). Effects of Low-Velocity Fault Damage  
827 Zones on Long-Term Earthquake Behaviors on Mature Strike-Slip Faults. *Journal of*  
828 *Geophysical Research: Solid Earth*. <https://doi.org/10.1029/2020JB019587>
- 829 Vidale, J., Helmberger, D. V., & Clayton, R. W. (1985). Finite-difference seismograms  
830 for SH waves. *Bulletin of the Seismological Society of America*.
- 831 Wang, Y., Allam, A. A., & Lin, F.-C. (2019). Imaging the Fault Damage Zone of the San  
832 Jacinto Fault Near Anza With Ambient Noise Tomography Using a Dense Nodal  
833 Array. *Geophysical Research Letters*. <https://doi.org/10.1029/2019GL084835>
- 834 Weertman, J. (1980). Unstable slippage across a fault that separates elastic media of  
835 different elastic constants. *Journal of Geophysical Research*, *85*(B3), 1455–1461.  
836 <https://doi.org/10.1029/JB085iB03p01455>

- 837 White, M. C., Fang, H., Catchings, R. D., Goldman, M. R., Steidl, J. H., & Ben-Zion, Y.  
838 (2020, 07). Detailed travelttime tomography and seismicity around the 2019 M7.1  
839 Ridgecrest, CA, earthquake using dense rapid-response seismic data. Poster  
840 Presentation at 2020 SCEC Annual Meeting.
- 841 Xu, S., Ben-Zion, Y., & Ampuero, J. P. (2012). Properties of inelastic yielding zones  
842 generated by in-plane dynamic ruptures-II. Detailed parameter-space study.  
843 *Geophysical Journal International*. [https://doi.org/10.1111/j.1365-](https://doi.org/10.1111/j.1365-246X.2012.05685.x)  
844 [246X.2012.05685.x](https://doi.org/10.1111/j.1365-246X.2012.05685.x)
- 845 Xu, X., Sandwell, D. T., & Smith-Konter, B. (2020). Coseismic displacements and  
846 surface fractures from sentinel-1 InSAR: 2019 Ridgecrest earthquakes.  
847 *Seismological Research Letters*, *91*(4), 1979–1985.  
848 <https://doi.org/10.1785/0220190275>
- 849 Zhu, L., & Kanamori, H. (2000). Moho depth variation in southern California from  
850 teleseismic receiver functions. *Journal of Geophysical Research: Solid Earth*,  
851 *105*(B2), 2969–2980. <https://doi.org/10.1029/1999JB900322>

852 Figure 1. Location map for the 2019 Ridgecrest earthquake sequence (colored  
853 circles, square, and stars) and four linear arrays (B1, B2, B3, and B4 as red, green,  
854 blue, and purple triangles, respectively) analyzed in this study. The catalog of  
855 Hauksson et al. (2012, extended to 2019) is used for earthquake locations, with color  
856 representing the focal depth (colorbar). Epicenters of the 2019 Mw 6.4 and Mw 7.1  
857 Ridgecrest earthquakes are marked as stars. Bandpass filtered waveforms, fault zone  
858 head waves, and fault zone trapped waves of an example event (orange square)  
859 recorded at array B4 are shown in Figs. S12, S13a, and 7a. Fault surface traces are  
860 depicted as black lines with ruptures of the 2019 Ridgecrest earthquake sequence  
861 being thicker. Near-fault seismic events outlined by the red box are analyzed in  
862 sections 3.2 and 3.3. The background gray colors indicate the local topography.  
863 WLSZ – Walker Lane Shear Zone; ECSZ – Eastern California Shear Zone; EF –  
864 Elsinore Fault; GF – Garlock Fault; SAF – San Andreas Fault; SJF – San Jacinto  
865 Fault.

866 Figure 2. Zoomed-in maps of all the Ridgecrest linear arrays (triangles) in (a) and  
867 B1-B4 in (b)-(e), respectively. Color of the map background depicts the surface  
868 geology (i.e., rock types; legend in (a)) extracted from the USGS website (see Data  
869 Availability). The station elevation is illustrated by the color of the triangles in (b)-  
870 (e). The green circle and black lines denote the center of the array and surface traces  
871 of faults associated with the 2019 Mw 7.1 and Mw 6.4 Ridgecrest earthquakes (red  
872 and blue stars), respectively. The green bars outline the span of the low-velocity  
873 zones identified in the local *P*-wave delay time analysis (Section 3.2), whereas the red  
874 bars illustrate the region of the slower inner cores (Fig. 6). The blue arrows depict the  
875 extent of the transition zone pointing from the slower to faster crustal blocks (black  
876 solid curves in Fig. 6).

877 Figure 3. (a) Locations of array B4 (triangle) and four teleseismic events analyzed  
878 in this study (stars), with the red star indicating the event analyzed in (b)-(c). (b) *P*  
879 waves recorded on vertical-component sensors of array B4 for the target teleseismic  
880 event are illustrated in colors with red and blue indicating positive and negative  
881 values. The *P*-wave arrival time predicted from the model IASP91 is used to align the

882 *P* waveforms and is set to be zero in the time axis. The *P* waveforms are bandpass  
 883 filtered twice. After applying a bandpass filter between 0.5 Hz and 2 Hz, the array-  
 884 mean envelope function and an array-mean *P*-wave pick are computed and depicted  
 885 as the curve and the vertical solid line in black, respectively. (c) Amplitude spectrum  
 886 averaged over the entire array with the red star and horizontal dashed lines indicating  
 887 the peak frequency and median of the amplitude spectrum between 0.5 Hz and 2 Hz,  
 888 respectively. Then, a second bandpass filter between the frequency range outlined by  
 889 the vertical dashed lines in (c) is applied. The red dashed curve in (b) depicts the  
 890 teleseismic *P*-wave delay times, measured using the *P* waveforms tapered between  
 891 the vertical dashed lines ( $\pm$  one dominant period relative to the array-mean *P*-wave  
 892 pick).

893 Figure 4. Teleseismic *P*-wave delay times for arrays (a) B1, (b) B2, (c) B3, and  
 894 (d) B4. The colored stars indicate *P*-wave delay times measured from different  
 895 teleseismic events and are labeled in the legend by the corresponding peak frequency  
 896 of the array-mean *P*-wave amplitude spectrum. The black dots depict the delay-time  
 897 pattern averaged over all teleseismic events, with error bars representing the standard  
 898 deviation of the mean. The blue and red dashed curves illustrate the delay times after  
 899 a topographic correction, assuming constant *P*-wave velocities of 2 km/s and 4 km/s.  
 900 The green bars outline the span of the low-velocity zones identified in local *P*-wave  
 901 delay time analysis (Section 3.2), while the red bars illustrate the region of the slower  
 902 inner cores (Fig. 6).

903 Figure 5. (a) *P* waveforms of an example local seismic event, shown as the blue  
 904 star in (c), recorded on vertical-component sensors of array B1. Waveform at each  
 905 station is normalized by its corresponding maximum amplitude and bandpass filtered  
 906 between 0.5 Hz and 20 Hz. Red stars denote the automatic *P* picks. (b) Same as (a)  
 907 but shown in slowness domain, i.e., the time axis of each station is divided by the  
 908 corresponding hypocentral distance. (c) Distribution of seismic events that pass the  
 909 selection criteria (Section 3.2.1) for array B1 (red triangles) are shown as circles with  
 910 color representing the focal depth. Events used in the delay time analysis (Section  
 911 3.2) for array B1 are outlined by the red box (Area1) and the results are shown in

912 Figs. 6a-b. Data from events outside the red box (Area2 and Area3) are also analyzed  
 913 (Figs. S8c-d). The black lines represent fault surface traces. Earthquakes that are  
 914 excluded from the delay-time analysis at array B1 are shown as grey dots.

915 Figure 6. Statistical analysis of local *P*-wave arrival patterns for all four arrays.  
 916 (a) Red dots illustrate the *P*-wave relative slowness variation within array B1,  
 917 averaged over 189 local seismic events with depth > 5 km and along-fault distance <  
 918 5 km relative to the array. The error bars represent a range of three standard  
 919 deviations of the mean about each respective mean value. The solid black lines depict  
 920 the contribution associated with a *P*-wave velocity contrast (~5.3% faster in the NE)  
 921 across the fault beneath the array. The corresponding mean *P*-wave delay time  
 922 variation is illustrated as the blue curve with dashed blue curves indicating the  
 923 uncertainties. (b) The *P*-wave delay time variation after removing the modeled cross-  
 924 fault velocity contrast (the solid black curve in (a)) is shown in blue for array B1. The  
 925 green dashed vertical lines outline the identified low velocity zone (LVZ), where *P*  
 926 waves are significantly delayed with respect to the background level (black dashed  
 927 line). The red dashed vertical lines denote the inner core of the LVZ, i.e., the  
 928 amplitude of the blue curve is large whereas its gradient is relatively small. The gray-  
 929 scale heat map of values for relative slowness and delay times after the cross-fault-  
 930 velocity-contrast correction obtained at each station for all analyzed events is  
 931 illustrated in (a) and (b), respectively. PDF – Probability Density Function. Results  
 932 for arrays B2, B3, and B4 are shown in (c)-(d), (e)-(f), and (g)-(h), respectively.

933 Figure 7. (a) Fault zone trapped waves (FZTWs) following the *S*-wave arrivals for  
 934 an example event (square in Fig. 1) observed at the fault-parallel component of array  
 935 B4. The waveforms are preprocessed following the steps of Figure S6 of Qiu et al.  
 936 (2017). The blue bar outlines the stations with FZTWs. (b) Red dots and blue stars  
 937 denote the distributions of normalized peak ground velocities (PGV) and root mean  
 938 square amplitudes (RMS) of the *S* waveforms shown in (a). The black curve  
 939 represents the likelihood of FZTW, i.e., the normalized multiplication of PGV and  
 940 RMS values, and is used to identify FZTW candidates.

941 Figure 8. *S*-wave amplification analysis for arrays B1-B4 in (a)-(d). Gray-scale  
942 heat maps of FZTW-likelihood values (e.g., black curve in Fig. 7b) computed at each  
943 station in the array for all analyzed events are shown. Red dots depict the likelihood  
944 curve averaged over all analyzed events. Error bars represent a range of two standard  
945 deviations of the mean about each respective mean value. The bottom green bar  
946 marks the low velocity zone (LVZ) identified from the local *P*-wave delay time  
947 analysis (green dashed lines in Fig. 6), whereas the red bar illustrates the slower inner  
948 core of the LVZ (red dashed lines in Fig. 6). The blue bar in (d) outlines the stations  
949 with FZTWs at array B4 (blue bar in Fig. 7a).

950 Figure 9. (a) Locations of earthquakes (gray dots) analyzed in section 3.3. FZTW  
951 candidates identified through template matching, with correlation coefficient greater  
952 than 0.85 marked as stars and color representing the focal depth. Red triangles denote  
953 the location of array B4. The along-fault cross section of seismicity (dots and stars)  
954 and array B4 (triangle) are shown in the top inset. (b) FZTWs recorded at stations  
955 B416-B423 for nine high-quality candidate events (red) with the highest correlation  
956 coefficients. The template waveforms (Fig. 7a) are shown in black. The array-mean *S*  
957 pick and correlation coefficient of each candidate event are labeled in the top left. (c)  
958 Comparison between FZTWs of the reference event (in black) and those averaged  
959 over all the high-quality candidate events (in red) observed between stations B416-  
960 B423.

961 Figure 10. Inversion results for FZTWs observed between stations B416-423,  
962 averaged over candidates shown in Figure 9a. (a) Comparison between synthetic  
963 waveforms (red) computed using the best-fitting model parameters (black dots in (b))  
964 and the observed FZTWs (in black). (b) Fitness values of fault-zone model  
965 parameters from the last 10 generations of the inversion (green dots). The best-fitting  
966 parameters (black circles) are displayed in each panel and used to generate the  
967 synthetic waveforms shown in (a). Black curve indicates the probability density  
968 function of model parameters shown as green dots.

969



Figure 1.

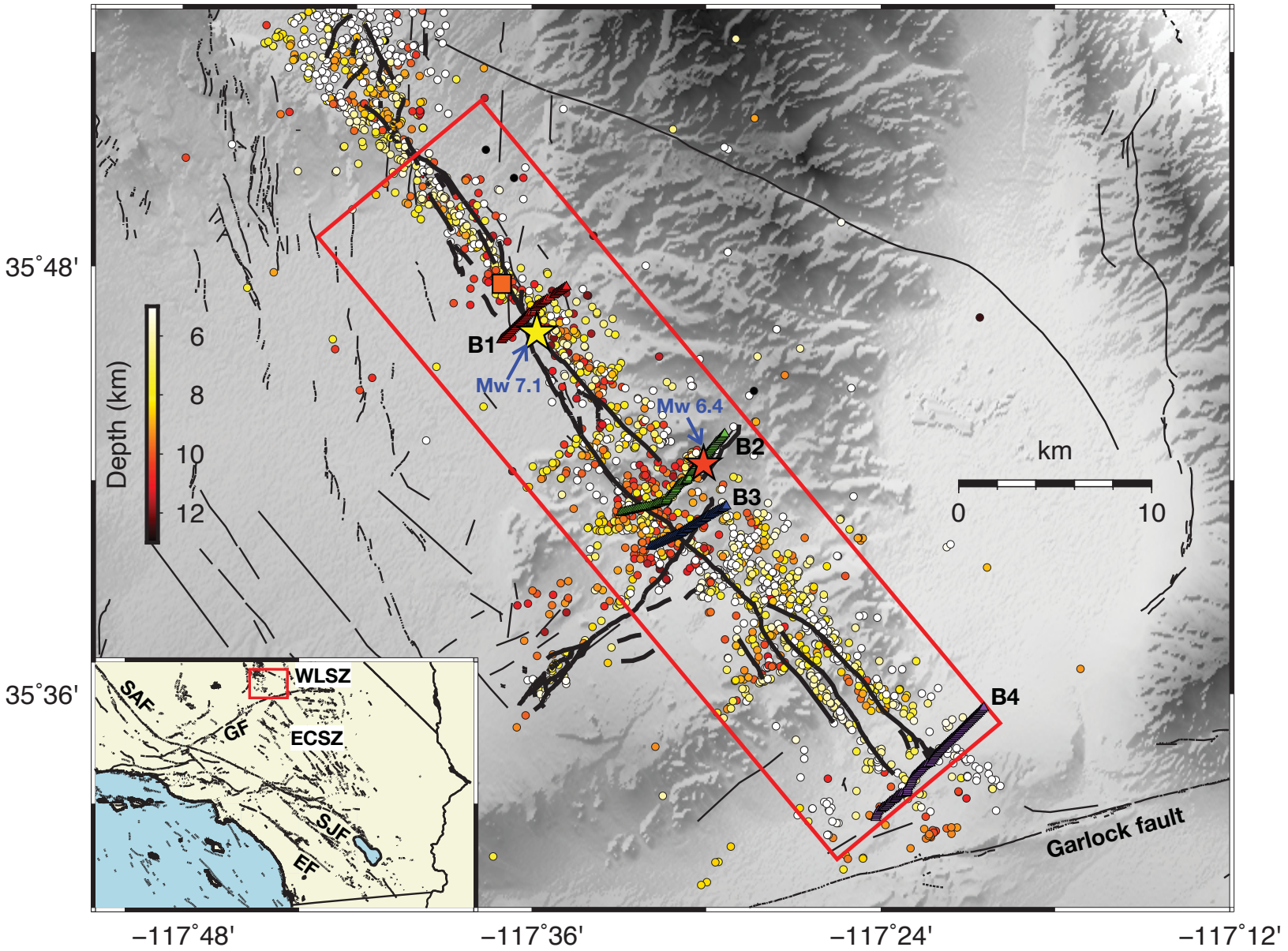


Figure 2.

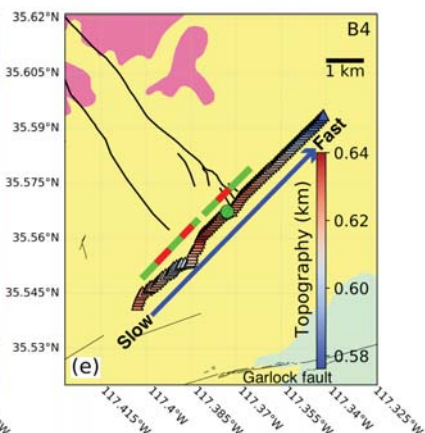
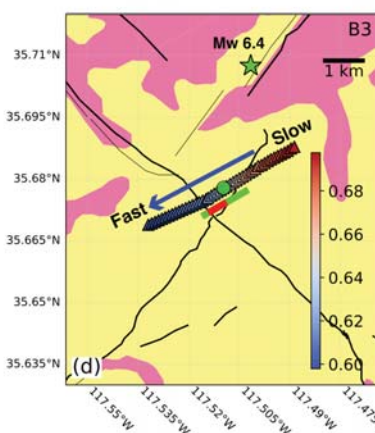
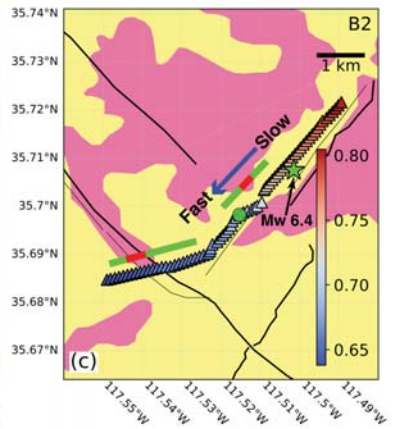
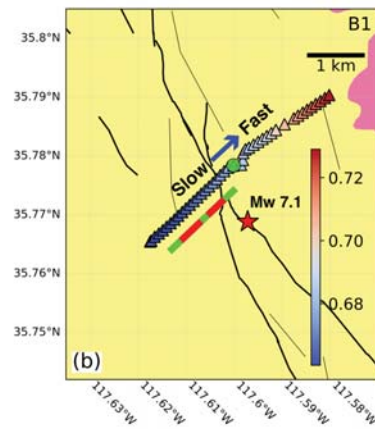
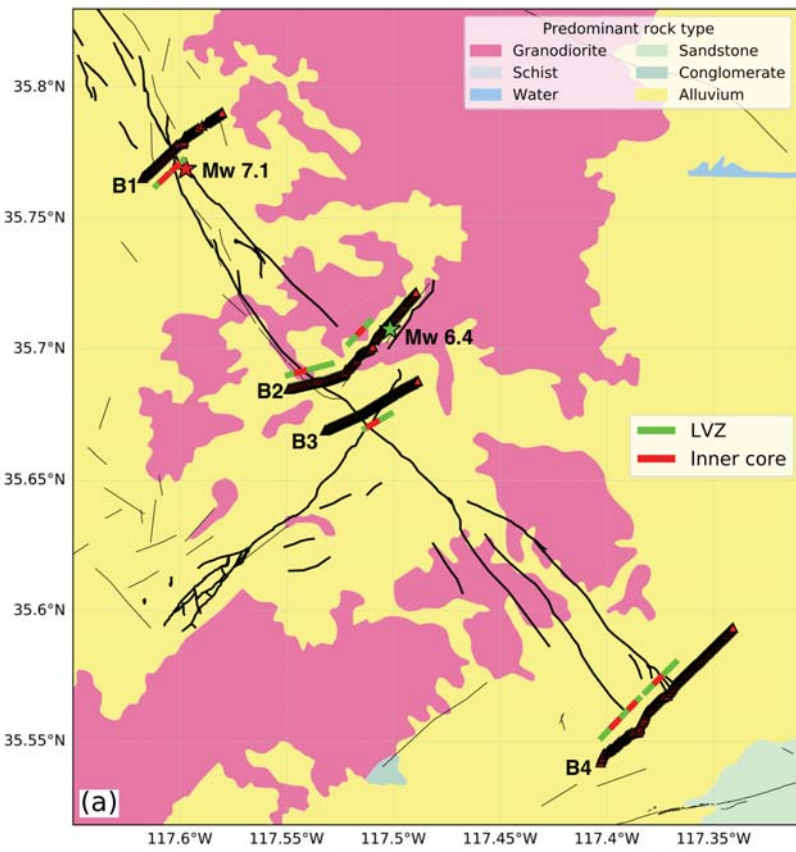
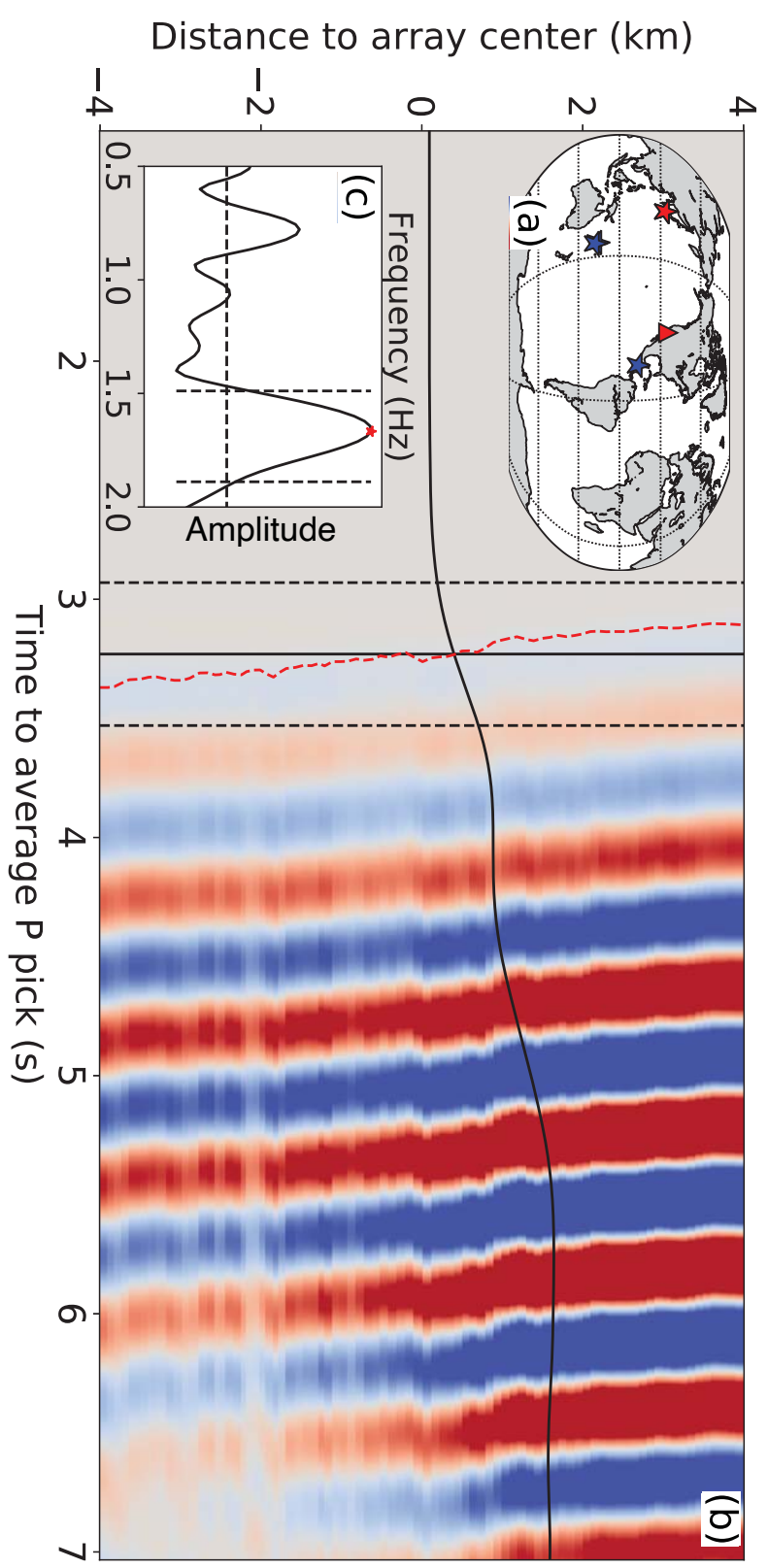


Figure 3.



**Figure 4.**

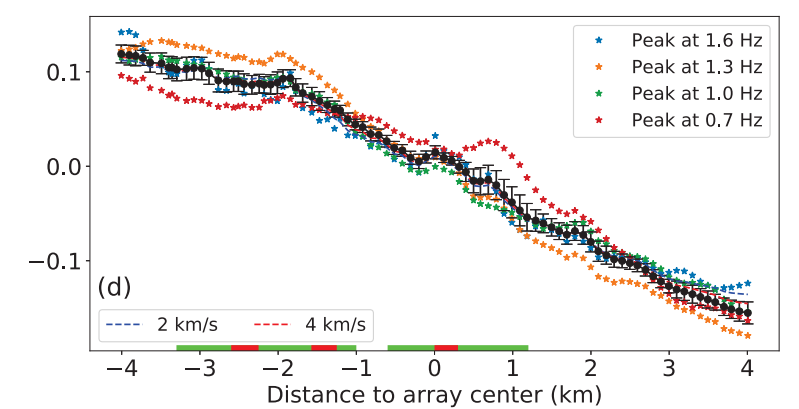
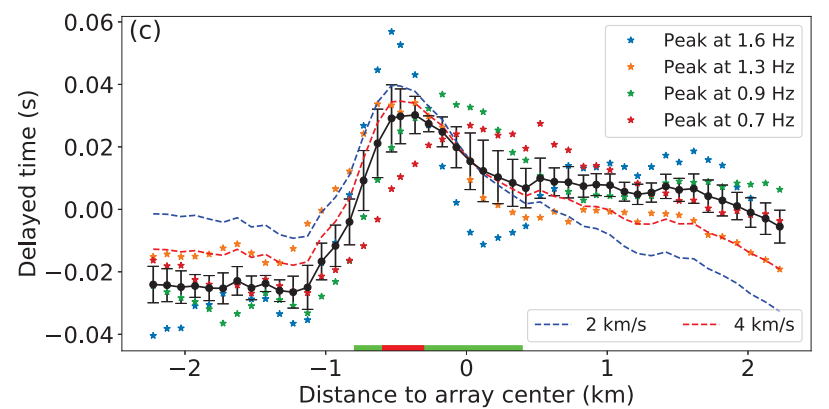
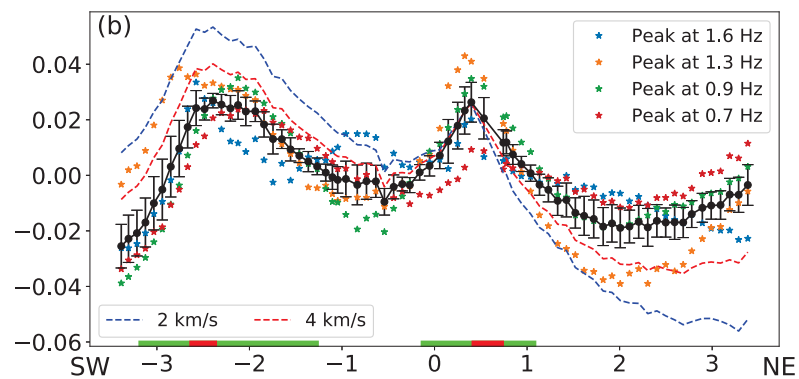
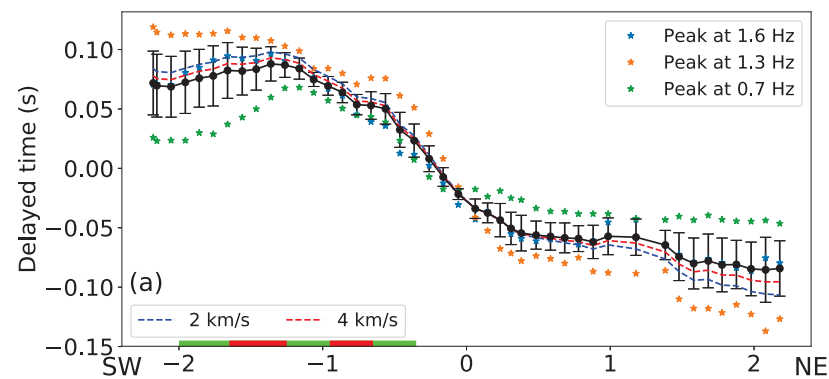




Figure 5.

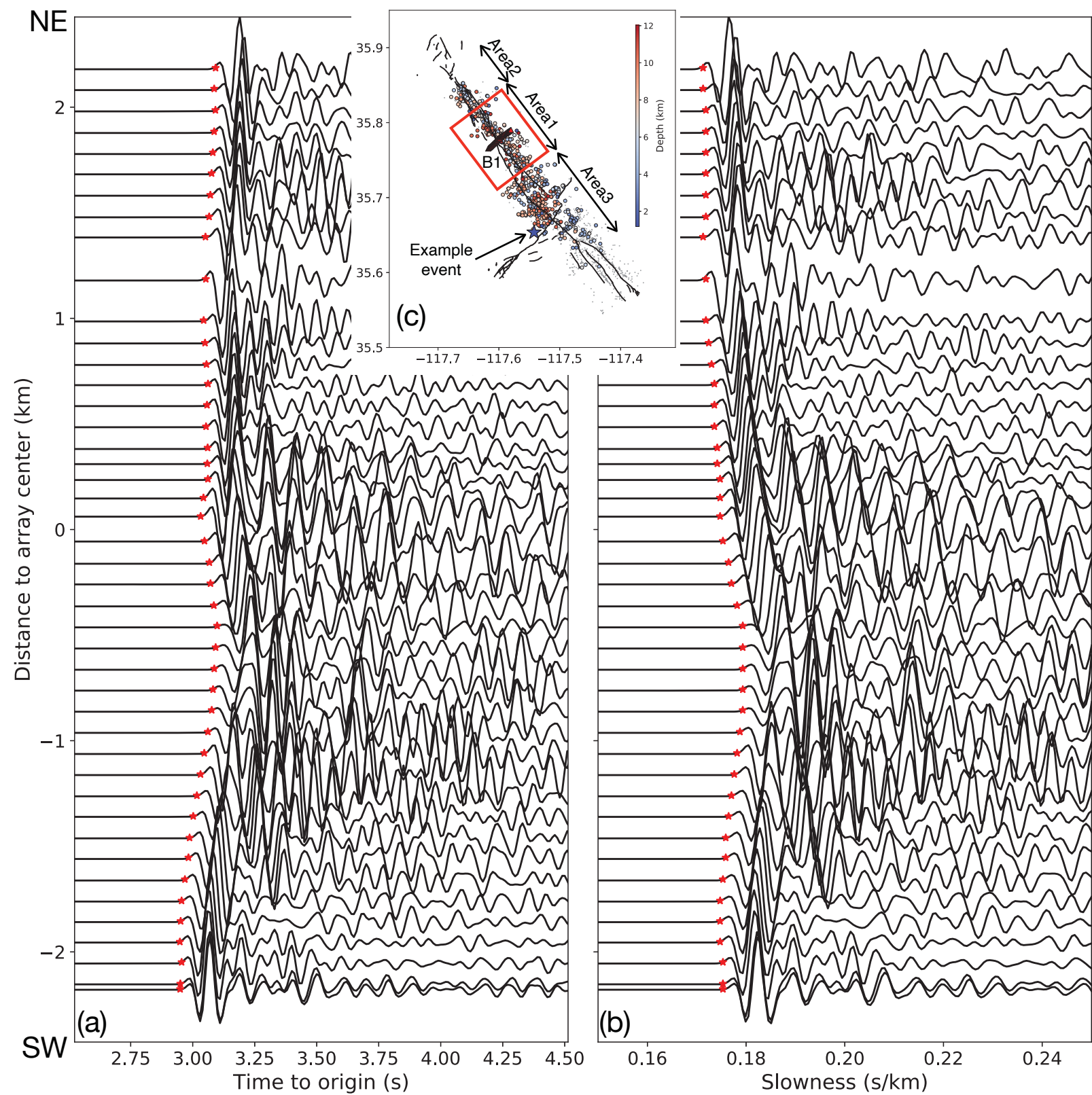


Figure 6.

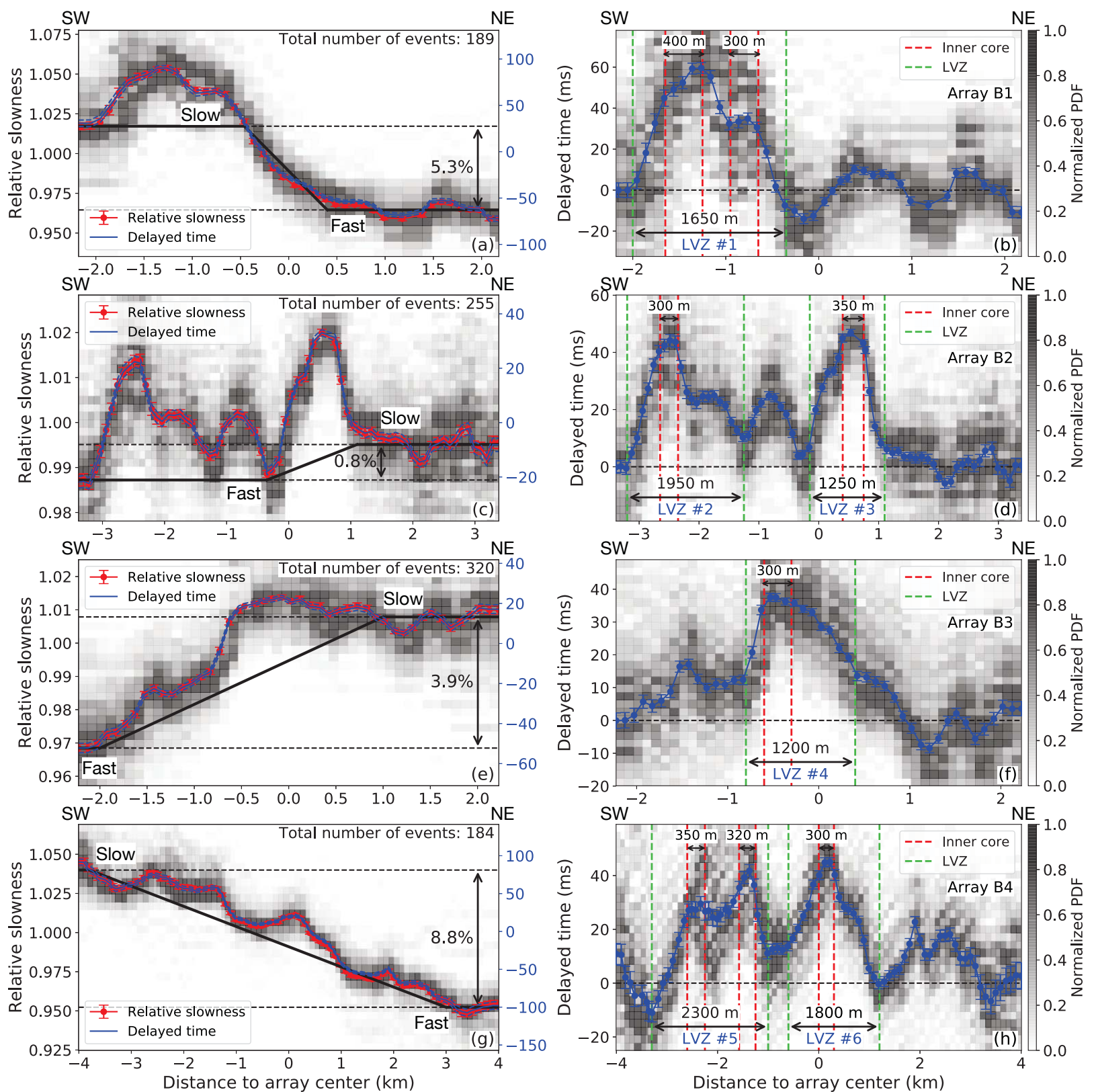


Figure 7.

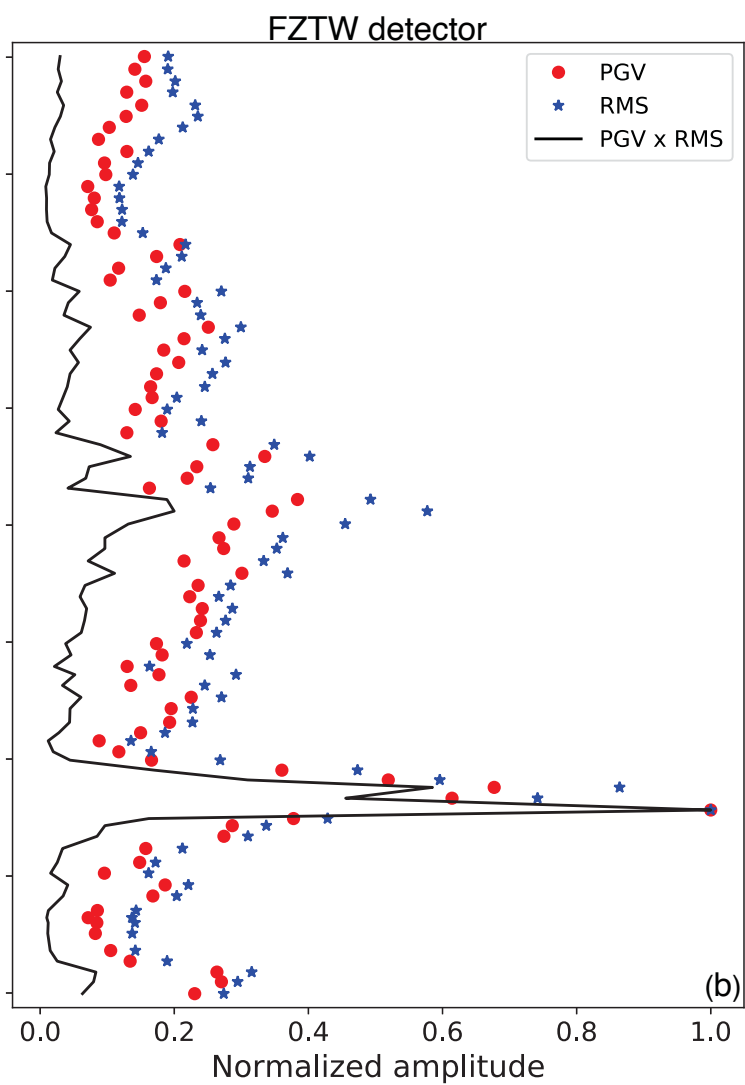
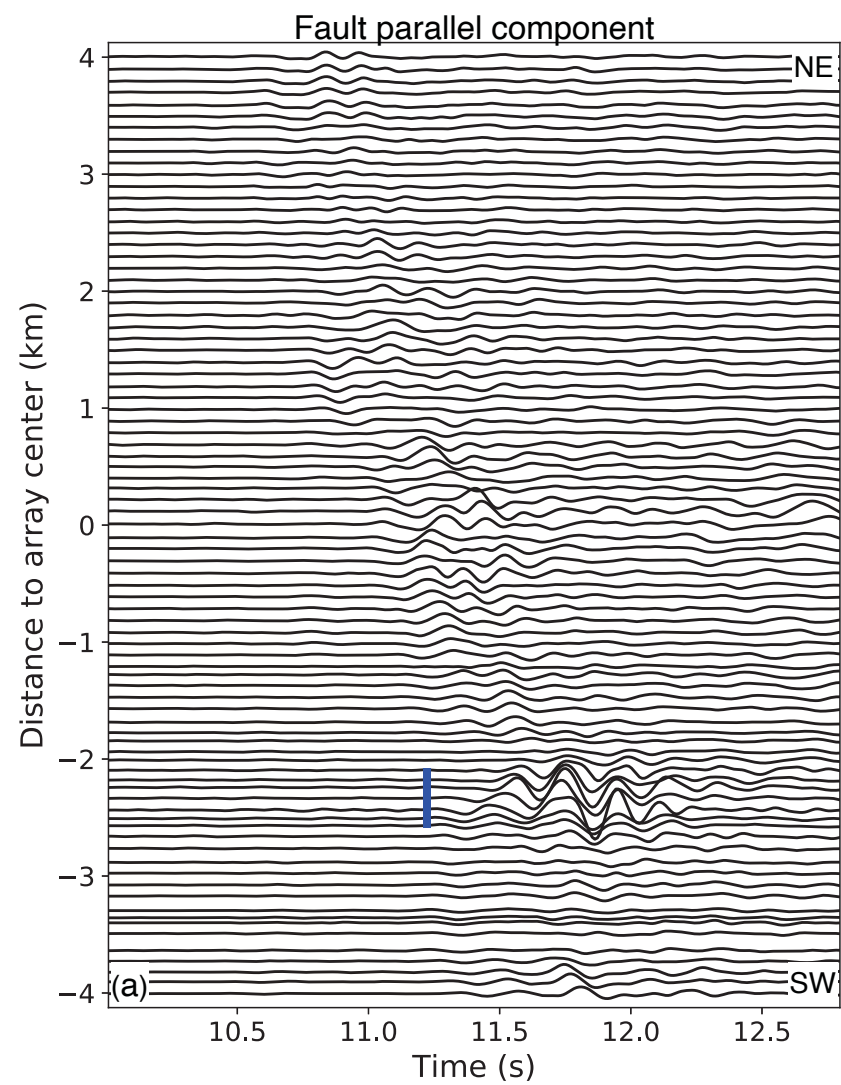


Figure 8.

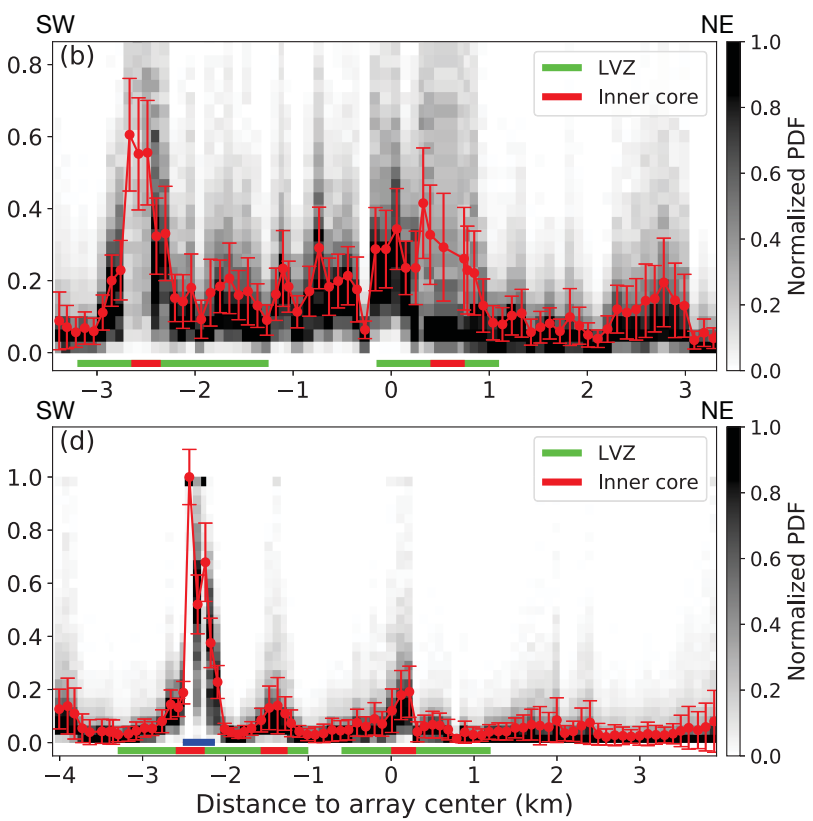
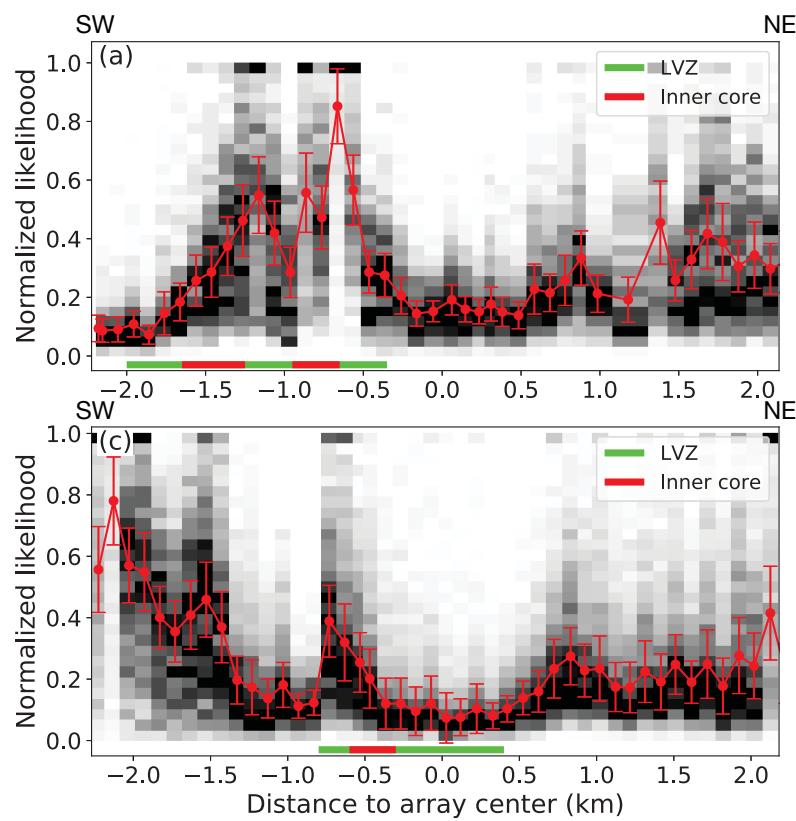




Figure 9.

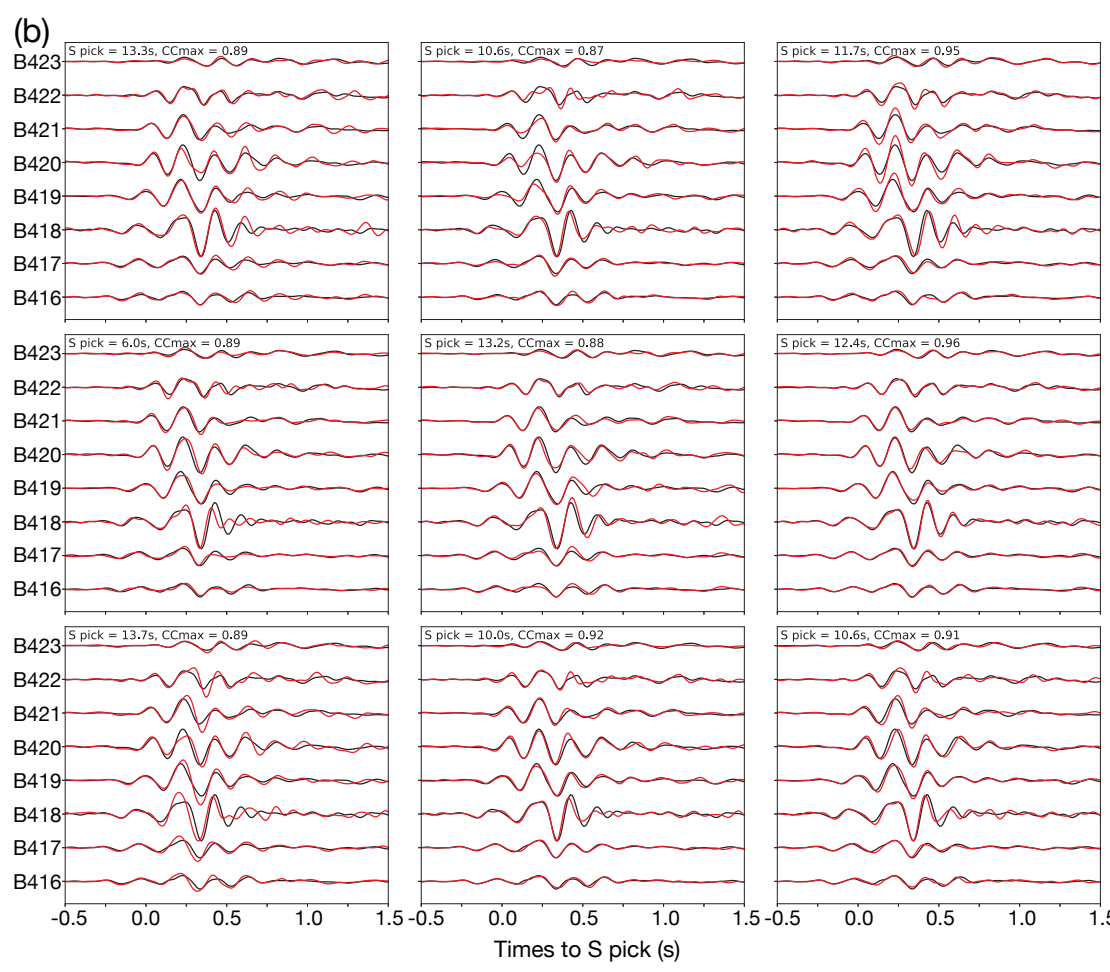
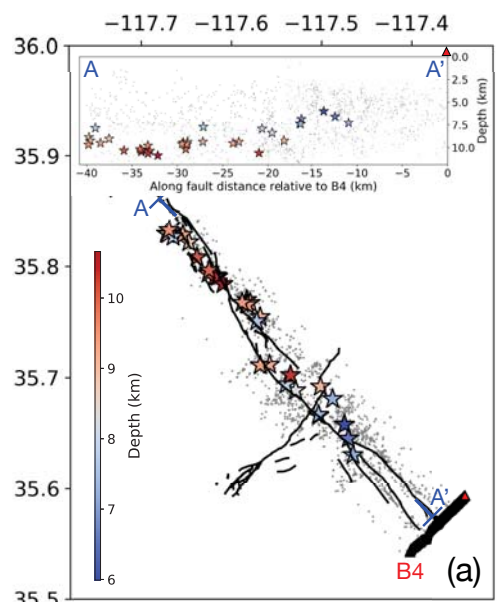


Figure 10.

